Journal of Non-Newtonian Fluid Mechanics 214 (2014) 88–105

Contents lists available at ScienceDirect

Journal of Non-Newtonian Fluid Mechanics

journal homepage: http://www.elsevier.com/locate/jnnfm

Viscoplastic Poiseuille flow in a rectangular duct with wall slip

Yiolanda Damianou, Georgios C. Georgiou *

Department of Mathematics and Statistics, University of Cyprus, P.O. Box 20537, 1678 Nicosia, Cyprus

ARTICLE INFO

Article history:
Received 28 July 2014
Received in revised form 1 September 2014
Accepted 5 October 2014
Available online 12 October 2014

Keywords:
Herschel–Bulkley fluid
Bingham plastic
Slip
Slip yield stress
Rectangular duct
Papanastasiou regularization

ABSTRACT

We solve numerically the Poiseuille flow of a Herschel–Bulkley fluid in a duct of rectangular cross section under the assumption that slip occurs along the wall following a slip law involving a non-zero slip yield stress. The constitutive equation is regularized as proposed by Papanastasiou. In addition, we propose a new regularized slip equation which is valid uniformly at any wall shear stress level by means of another regularization parameter. Four different flow regimes are observed defined by three critical values of the pressure gradient. Initially no slip occurs, in the second regime slip occurs only in the middle of the wider wall, in the third regime slip occurs partially at both walls, and eventually variable slip occurs everywhere. The performance of the regularized slip equation in the two intermediate regimes in which wall slip is partial has been tested for both Newtonian and Bingham flows. The convergence of the results with the Papanastasiou regularization parameter has been also studied. The combined effects of viscoplasticity and slip are then investigated. Results are presented for wide ranges of the Bingham and slip numbers and for various values of the power-law exponent and the duct aspect ratio. These compare favorably with available theoretical results and with numerical results in the literature obtained with both regularization and augmented Lagrangian methods.

1. Introduction

The class of viscoplastic fluids, i.e. fluids with yield stress, includes materials of industrial importance, such as slurries, suspensions, pastes, various food and pharmaceutical products, biofluids (e.g., blood), and geomaterials (e.g., lava and crude oil). A viscoplastic material behaves like a solid when it is not sufficiently stressed and flows like a fluid when the yield stress is exceeded. The simplest viscoplastic constitutive equation is that of the Bingham plastic, which is generalized to the Herschel–Bulkley constitutive equation [1,2]:

$$\begin{cases} \dot{\boldsymbol{\gamma}} = \mathbf{0}, & \tau \leqslant \tau_0 \\ \boldsymbol{\tau} = \left(\frac{\tau_0}{\dot{\gamma}} + k\dot{\gamma}^{n-1}\right)\dot{\boldsymbol{\gamma}}, & \tau \geqslant \tau_0 \end{cases} \tag{1}$$

where τ_0 is the yield stress, k is the consistency index, n is the power-law exponent, $\dot{\boldsymbol{\gamma}} \equiv \nabla\mathbf{u} + (\nabla\mathbf{u})^T$ is the rate of strain tensor, $\mathbf{u}$ is the velocity vector, and the superscript T denotes the transpose. The magnitudes of $\boldsymbol{\tau}$ and $\dot{\boldsymbol{\gamma}}$, denoted respectively by τ and $\dot{\gamma}$, are defined by

$$\dot{\gamma} \equiv \sqrt{\frac{1}{2}\mathrm{II}_{\dot{\gamma}}} = \sqrt{\frac{1}{2}\dot{\boldsymbol{\gamma}} : \dot{\boldsymbol{\gamma}}} \quad \text{and} \quad \tau \equiv \sqrt{\frac{1}{2}\mathrm{II}_{\tau}} = \sqrt{\frac{1}{2}\boldsymbol{\tau} : \boldsymbol{\tau}} \tag{2}$$

where the symbol II stands for the second invariant of a tensor. For $n = 1$, Eq. (1) is reduced to the Bingham plastic model and k denotes the plastic viscosity. Other viscoplastic constitutive models are also used, such as the Casson model [1].

To solve a viscoplastic flow one needs to overcome the difficulty of determining the yielded regions, i.e. regions in the flow domain where $\tau > \tau_0$ and thus the material deforms, and the unyielded regions, where $\tau \leqslant \tau_0$. Unyielded regions include zones where the material moves undeformed as a rigid body and dead zones where it is stagnant. There are two main approaches in resolving the above difficulty: (a) using augmented Lagrangian methods (ALMs) which are based on variational inequalities; and (b) using regularization methods. The ALMs are based on the variational formulation of the Navier–Stokes equations and employ optimization algorithms to determine the flow solution [2]. In the second approach, the constitutive equation is actually modified by introducing an additional parameter in order to combine the two branches of Eq. (1) into one smooth (differentiable) function, so that the resulting regularized equation applies everywhere in the flow field in both yielded and (practically) unyielded regions. The most popular regularization in the literature is that proposed by Papanastasiou [3]:

$$\boldsymbol{\tau} = \left\{\frac{\tau_0[1 - \exp(-m\dot{\gamma})]}{\dot{\gamma}} + k\dot{\gamma}^{n-1}\right\}\dot{\boldsymbol{\gamma}} \tag{3}$$

* Corresponding author. Tel.: +357 22892612; fax: +357 22895352.
E-mail address: georgios@ucy.ac.cy (G.C. Georgiou).

http://dx.doi.org/10.1016/j.jnnfm.2014.10.002
0377-0257/

where m is the stress growth exponent. For sufficiently large values of the parameter m, the above model provides a satisfactory approximation of the Herschel–Bulkley model. Other regularized models, e.g., that proposed by Bercovier and Engelman [4], have been reviewed by Frigaard and Nouar [5]. The advantages and disadvantages of the two main approaches have also been recently reviewed by Balmforth et al. [2]. The regularized approach is easier to implement but eliminates yield surfaces replacing unyielded regions with regions of very high viscosity. The "unyielded" areas are determined as the areas where $\tau \leqslant \tau_0$ (von Mises criterion) or the areas where the strain rate is small.

Conduit flows of viscoplastic materials are of importance in the processing or transport of slurries, suspensions or pastes and also find applications in geophysical, debris, and glacier flows [6]. A number of researchers have studied the two-dimensional flow of Bingham or Herschel–Bulkley fluids in rectangular ducts using different methods. Mosolov and Miasnikov [7–9] analysed mathematically the steady-state flow of Bingham plastics in a pipe of an arbitrary cross-section and proved existence and uniqueness theorems for the solution. They established the existence of a rigid core region and of stagnant regions near corners with convex boundaries toward the corners. They also obtained interesting results for the shape of the unyielded zones in the flow field and the critical value of the pressure gradient below which the flow stops. Atkinson and El-Ali [10] carried out a local analysis of pressure-driven Bingham flow near corners and showed the possible existence of 'plug' regions in the neighbourhood of acute corners. Based on the pioneering work of Mosolov and Miasnikov [7], Huilgol [11] developed a systematic procedure to determine the critical pressure gradient for the initiation of viscoplastic flow as well as the shape of the yield surface when the flow is about to commence in pipes of symmetric cross-section (including rectangular ducts). He also showed that the Mosolov–Miasnikov approach applies to all viscoplastic fluids with a constant yield stress, such as Herschel–Bulkley and Casson fluids.

Taylor and Wilson [6] solved numerically the Bingham flow in rectangular ducts by means of finite differences using the regularization of the constitutive equation proposed by Bercovier and Engelman [4]. They noted, however, that their numerical scheme could not work for small values of the regularization parameter. As a consequence, the computed yielded and unyielded regions were not converged. Taylor and Wilson [6] pointed out that in agreement with theory there may be stagnant regions at the corners depending on the flow parameters. However, due to the inaccuracies in the solution the concavity of the dead regions is reversed and the latter regions may merge with the rigid ones in the center of the duct [12]. Stagnant regions were previously obtained by Huilgol and Panizza [13] who used variational inequalities to solve the Poiseuille flow of a Bingham plastic through a duct of an L-shaped cross-section. They reported that the stagnant zones are near acute-angled corners in agreement with the theoretical predictions of Atkinson and El-Ali [10]. Pham and Mitsoulis [14] solved Bingham plastic flows in ducts of various cross-sections using the Papanastasiou regularization. However, their results for flow in a square duct were similar to those of Taylor and Wilson [6] due to the low value of the regularization parameter employed.

Wang [15] studied the duct flow of generalized viscoplastic fluids in a square duct and in eccentric annuli using a finite element method and tracking the yield surface by means of a regularization technique based on the theory of variational inequalities. He reported that the plug zones are almost identical for various plastic models despite their different shear-thinning behavior. Accurate solutions of the steady-state Poiseuille flow of a Bingham fluid in the case of a square duct were obtained by Saramito and Roquet [16] by means of a new mixed anisotropic auto-adaptive finite element method coupled with the augmented Lagrangian algorithm. Saramito and Roquet [16] also noted that while the ALM is used to solve the ideal Bingham flow, using the finite element method for calculating the yield surface is not necessarily very precise. According to Faria and Karam-Filho [7], one needs to resort to higher-order approximations and/or mesh refinement, which lead to a fast increase of the computational cost, while the accuracy of the yield surface is improved rather slowly. The above difficulties are overcome using the "regularization technique" [17]. Huilgol and You [18] applied the ALM to the steady-state flow problems of Bingham, Casson, and Herschel–Bulkley fluids in pipes of circular and square cross sections. Steady-state and time-dependent studies of Bingham flow (start-up and cessation) in ducts of various cross-sections have been carried out by Muravleva and Muravleva [19,20].

Viscoplastic materials are dispersed systems known to exhibit wall slip, which arises due to the depletion of particles adjacent to the shearing surface ([21–23] and references therein). Wall slip may have profound effects on the flow of complex materials [22]. The experimental data show that the slip velocity u_w, defined as the relative velocity of the fluid with respect to that of the wall, depends on the wall shear and normal stresses, the temperature, the properties of the material (e.g. molecular weight and its distribution in polymers or particle size and concentration in suspensions, etc) and the fluid/wall interface [24]. The simplest slip equation is the Navier-slip law which can be written as follows

$$\tau_w = \beta u_w \tag{4}$$

where τ_w is the wall shear stress and β is the slip coefficient, which includes the effects of all other factors mentioned above (e.g., that of temperature). The no-slip and the perfect-slip cases are obtained for $\beta \to \infty$ and $\beta = 0$, respectively.

In the present work, the following generalized slip model is employed

$$\begin{cases} u_w = 0, & \tau_w \leqslant \tau_c \\ \tau_w = \tau_c + \beta u_w, & \tau_w > \tau_c \end{cases} \tag{5}$$

where τ_c is the slip yield stress, i.e. the critical value that should be exceeded by the wall shear stress for slip to occur. Experimental data on different fluid systems, ranging from Newtonian systems to colloidal suspensions, supporting the existence of a non-zero slip yield stress have been compiled in Ref. [25]. When $\tau_c = 0$ the Navier slip condition is recovered. In fact, Eq. (5) is the scalar analog of the equation used by Fortin et al. [26] for sample numerical simulation of Bingham flows, such as the round Poiseuille flow and the sudden contraction flow. A more general form of Eq. (5), involving a power-law exponent for the slip velocity was earlier proposed by Yilmazer and Kalyon [27] to describe the behavior of viscoplastic materials, namely highly filled suspensions, in capillary and parallel disk torsional flows.

Given that it is not always known a priori which branch applies, using the discontinuous Eq. (5) poses difficulties similar to those encountered with the ideal Bingham constitutive model. For

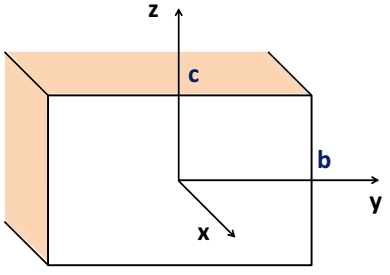

Fig. 1. Geometry of the rectangular tube.

example, in one-dimensional planar and axisymmetric Poiseuille flows, slip occurs only above a critical value of the pressure gradient, which separates the no-slip from the slip regime [28]. One then needs to calculate first this critical value in order to construct the two-branch flow curve. The situation becomes more complex in two-dimensional flows: slip may occur only along certain parts of the wall and the points where there is a change in the branch of the slip equation are part of the problem, which cannot be determined analytically even for Newtonian flows [28]. Roquet and Saramito [29] noted that the determination of the parts of the wall where the material slips or sticks is of practical importance in extrusion and for earth cracks.

Fortin et al. [26] pointed out the analogy between Eqs. (5) and (1) and applied the augmented Lagrangian method, i.e. variational inequalities, to impose slip Eq. (5) together with the ideal Bingham plastic constitutive equation. Roquet and Saramito [29], who employed the term "stick–slip" for the slip boundary condition (5), used the same method to solve the Newtonian Poiseuille flow in a duct. The localization of the stick–slip transition points was approximated by an anisotropic auto-adaptive mesh procedure. In a subsequent work, they obtained systematic results for Bingham flow in a square duct over wide ranges of values for τ_0 and τ_c [30].

Damianou et al. [31] followed the regularization approach for the power-law generalization of Eq. (5) in their study of the cessation of axisymmetric Poiseuille flow of a Herschel–Bulkley fluid. The regularized version of Eq. (5) is as follows:

$$\tau_w = \tau_c[1 - \exp(-m_c u_w)] + \beta u_w \tag{6}$$

where m_c is a growth parameter similar to the stress growth exponent of the Papanastasiou model. Equation (6) is valid uniformly at any wall shear stress level and is easy to use in numerical simulations. Damianou et al. [31] showed that for sufficiently large values of m_c, Eq. (6) performs well and provides a satisfactory approximation of Eq. (5). In particular, they showed that in the case of Navier slip (i.e. for zero slip yield stress), the fluid slips at all times, the velocity becomes and remains uniform before complete cessation, and the stopping time is finite only when the slip exponent is less than unity; otherwise, the stopping time is infinite for any non-zero Bingham number and the volumetric flow rate decays exponentially. When the slip yield stress is non-zero, slip ceases at a finite critical time, the velocity becomes flat only in complete cessation, and the stopping times are finite, in agreement with theoretical estimates.

In most experimental studies on various materials τ_c appears to be much lower than τ_0 [32–34]. In general, the relative values of τ_c and τ_0 may lead to different flow situations. For example, one of these material parameters may be zero, which leads to the special cases of a non-viscoplastic fluid exhibiting wall slip with non-zero slip yield stress ($\tau_0 = 0$, $\tau_c \neq 0$) and of a viscoplastic fluid exhibiting no- or Navier slip ($\tau_0 \neq 0$, $\tau_c = 0$). Even in the ideal case where the two material parameters are constant, different flow regimes can be observed depending on their relative values. Hence, in round Poiseuille flow, if $\tau_c > \tau_0$, three regimes can be identified, defined by two critical values G_1 and G_2 for the imposed pressure gradient G: (a) for $G \leqslant G_1$ no flow occurs; (b) for $G_1 < G \leqslant G_2$, the material flows without slip and a central rigid zone appears the radius of which is reduced with the pressure gradient; (c) for $G > G_2$, the material flows with wall slip. Another possibility is to have $0 < \tau_c < \tau_0$, in which case there again exist three flow regimes: (a) for $G \leqslant G_1$, no flow occurs; for $G_1 < G \leqslant G_2$, all the material moves as rigid body (with a speed equal to the slip velocity); (c) for $G > G_2$, we have flow with slip with only a central unyielded rigid-body zone the radius of which decreases with the imposed pressure gradient. It should be noted, however, that using a global slip law in all regimes may be very simplistic, since in certain systems different slip behavior is observed for different slip values [22].

The objective of the present work is twofold. First we would like to solve numerically the flow of Newtonian and viscoplastic fluids in a rectangular duct assuming that wall slip with non-zero slip yield stress occurs and to test the performance of the regularized slip equation (5) in a two dimensional flow problem (so far this has been tested in 1D Poiseuille flows). Second, to study systematically the performance of the Papanastasiou-regularized version of the Herschel–Bulkley constitutive equation in this unidirectional two-dimensional flow with wall slip. Using the regularization approach for both the constitutive and the slip equations for solving Herschel–Bulkley flow in a rectangular duct are not the only differences of the present work from that of Roquet and Saramito [29,30] who solved both the Newtonian and the Bingham flow in a square duct with the augmented Lagrangian method. These authors chose to fix the slip number (i.e. the dimensionless number corresponding to the slip coefficient β) and varied τ_c, as well as τ_0 in the Bingham case, in order to identify different flow regimes with complex flow patterns. In the present work, the Newtonian flow is systematically analyzed for different values of the slip coefficient, flow curves are constructed, and the different flow regimes are identified in terms of the imposed pressure gradient. In the Bingham flow case, we assume that $\tau_c = \tau_0$ and vary both τ_0 and β, in order to investigate the different viscoplastic flow patterns in the presence of weak, moderate, and strong slip with non-zero slip yield stress.

The rest of the paper is organized as follows. In Section 2 the governing equations of the flow are presented. In Section 3, we summarize the analytical solution for the Newtonian Poiseuille flow in the case of slip with non-zero slip yield stress, which was derived by Kaoullas and Georgiou [28]. It should be noted that the flow problem is amenable to analytical solution only below the critical pressure required for the initiation of slip along the wider wall and above a second critical pressure gradient needed for the occurrence of (non-uniform) slip everywhere along both walls. Numerical solutions in these regimes but also in the intermediate regime for which there is no analytical solution are presented and discussed in Section 4, which is devoted to the Newtonian flow. It is shown that the regularized slip Eq. (6) performs well in this two-dimensional flow problem and that for sufficiently high values of the growth parameter the discontinuous wall slip velocity is predicted accurately. In Section 5, results for the Herschel–Bulkley flow are presented. The effect of the Papanastasiou parameter is analyzed in the no-slip case. The cases of Navier slip

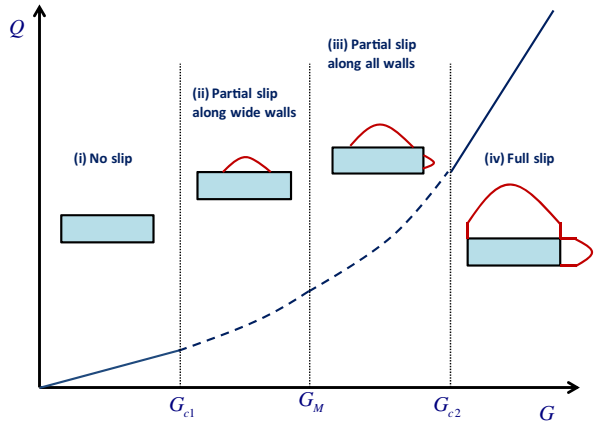

Fig. 2. Sketch showing the various flow regimes of Poiseuille flow in a rectangular duct with wall slip and non-zero slip yield stress. G is the imposed pressure gradient and Q is the resulting volumetric flow rate.

and of non-zero slip yield stress with $\tau_c = \tau_0$ are then analyzed and discussed. Finally, in Section 6 the main conclusions of this work are summarized.

2. Governing equations

We consider the steady state, creeping Poiseuille flow in a duct of rectangular cross-section and infinite length with $-b \leqslant y \leqslant b, -c \leqslant z \leqslant c$, where $b \geqslant c$, as shown in Fig. 1. Only the first quadrant is considered due to the symmetry with respect to the planes $y = 0$ and $z = 0$. The flow is governed by the momentum equation

$$\nabla \cdot \boldsymbol{\tau} = -G \tag{7}$$

where G is the pressure gradient and $\boldsymbol{\tau}$ is the viscous stress tensor. In the present work $\boldsymbol{\tau}$ is given by the regularized Herschel–Bulkley constitutive Eq. (3). To non-dimensionalize the governing equations we scale the velocity and the pressure by appropriate scales, denoted by V_s and P_s, respectively, and lengths by c. Hence the flow domain becomes $-\alpha \leqslant y^* \leqslant \alpha, -1 \leqslant z^* \leqslant 1$, where the stars denote dimensionless variables and $\alpha \equiv b/c \geqslant 1$ is the aspect ratio of the duct.

In the case the volumetric flow rate is imposed, the mean velocity V in the duct is used as the velocity scale, i.e. $V_s = V$, and we take $P_s = k(V/c)^n$. The non-dimensionalized forms of the momentum, constitutive, and slip equations, given respectively by (7), (3) and (6), are

$$\nabla \cdot \boldsymbol{\tau}^* = -G^* \tag{8}$$

$$\boldsymbol{\tau}^* = \left\{ \frac{Bn[1 - \exp(-M\dot{\gamma}^*)]}{\dot{\gamma}^*} + \dot{\gamma}^{*n-1} \right\} \dot{\boldsymbol{\gamma}}^* \tag{9}$$

and

$$\tau_w^* = B_c[1 - \exp(-M_c u_w^*)] + Bu_w^* \tag{10}$$

In the dimensionless constitutive Eq. (9) there appear two dimensionless numbers, the Bingham number, Bn, and the dimensionless stress growth number, M, defined by

$$Bn \equiv \frac{\tau_0 c^n}{kV} \quad \text{and} \quad M \equiv \frac{mV}{c} \tag{11}$$

Three additional dimensionless numbers appear in the slip Eq. (10): the slip-yield-stress number, B_c, the slip number, B, and the growth number, M_c, defined as follows:

$$B_c \equiv \frac{\tau_c c^n}{kV}, \quad B \equiv \frac{\beta c^n}{kV^{n-1}}, \quad M_c \equiv m_c V \tag{12}$$

When the pressure gradient is imposed, we take $V_s = c(\tau_0/k)^{1/n}$ and $P_s = \tau_0$. It turns out that the dimensionless forms of the governing equations are identical to (8)–(10), the only differences being that the Bingham number does not appear ($Bn = 1$) and the other dimensionless numbers are defined by

$$M \equiv m\left(\frac{\tau_0}{c}\right)^{1/n}, \quad B_c \equiv \frac{\tau_c}{\tau_0}, \quad B \equiv \frac{\beta c}{\tau_0}\left(\frac{\tau_0}{k}\right)^{1/n}, \quad M_c \equiv m_c c\left(\frac{\tau_0}{k}\right)^{1/n} \tag{13}$$

It should be noted that in the case of Bingham flow ($n = 1$), the definitions of the slip number are the same in both non-dimensionalizations.

3. Analytical solution for Newtonian flow

The analytical solution of the Newtonian flow with non-zero slip yield stress is given in [28]. It is conveniently summarized here in order to introduce the various flow regimes that appear in the case of a rectangular duct and the associated critical values of the pressure gradient. In the next section, it will also be used in testing the numerical code. In the case of Newtonian flow in a rectangular duct, Eq. (7) is simplified to

$$\frac{\partial^2 u_x}{\partial y^2} + \frac{\partial^2 u_x}{\partial z^2} = -\frac{G}{\eta} \tag{14}$$

where η is the viscosity. In the case of zero slip yield stress, non-uniform slip occurs everywhere along the walls for any non-zero value of the pressure gradient. In the case of non-zero slip yield stress, there is no wall slip below a critical pressure gradient G_{c1}. Hence, for $G \leqslant G_{c1}$ the velocity is the standard-textbook, no-slip solution

$$u_x(y,z) = \frac{2Gc^2}{\eta} \sum_{i=1}^{\infty} \frac{(-1)^{i+1}}{\alpha_i^3} \cos(\alpha_i z/c) \left[1 - \frac{\cosh(\alpha_i y/c)}{\cosh(\alpha_i \alpha)}\right] \tag{15}$$

where $\alpha_i = (2i-1)\pi/2, i = 1, 2, \ldots$ are the eigenvalues of the problem. The volumetric flow rate for $G \leqslant G_{c1}$ is

$$Q = \frac{8Gbc^3}{\eta} \sum_{i=1}^{\infty} \frac{\alpha_i - \tanh(\alpha_i \alpha)/\alpha}{\alpha_i^4} \tag{16}$$

The wall shear stresses along the walls $y = b$ and $z = c$ are respectively given by

$$\tau_{wy}(z) = 2cG \sum_{i=1}^{\infty} \frac{(-1)^{i+1}}{\alpha_i^2} \tanh(\alpha_i \alpha) \cos(\alpha_i z/c) \tag{17}$$

and

$$\tau_{wz}(y) = 2cG \sum_{i=1}^{\infty} \frac{1}{\alpha_i^2} \left[1 - \frac{\cosh(\alpha_i y/c)}{\cosh(\alpha_i \alpha)}\right] \tag{18}$$

The maximum wall shear stress occurs at the middle of the wider wall ($z = c$) of the rectangular duct. Hence, slip occurs first along this wall. The pressure gradient G_{c1} below which no slip occurs corresponds to $\tau_{wz,max} = \tau_{wz}(0) = \tau_c$. Hence,

$$G_{c1} = \frac{\tau_c}{2c \sum_{i=1}^{\infty} \frac{1}{\alpha_i^2} [1 - \operatorname{sech}(\alpha_i \alpha)]} \tag{19}$$

When now the pressure gradient exceeds G_{c1}, slip initially occurs only in the middle of the wider wall. As the pressure gradient increases, slip also occurs in the middle of the narrower wall above

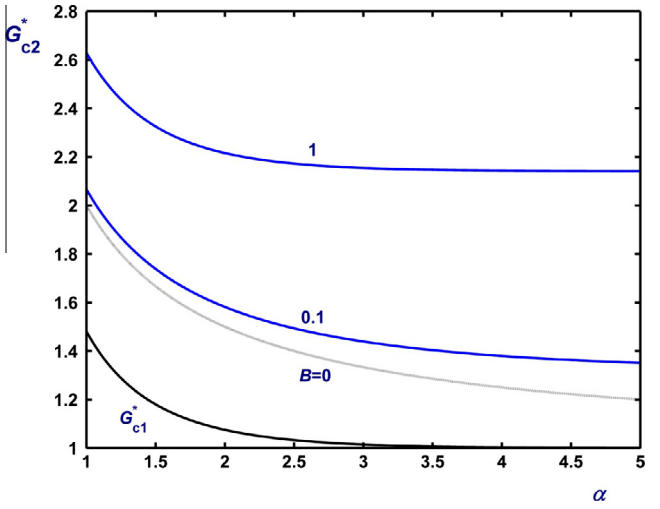

Fig. 3. Variation of G^*_{c2} with the aspect ratio α for various slip numbers in the case of Newtonian Poiseuille flow with non-zero slip yield stress. The first critical pressure gradient G^*_{c1}, which is independent of B, is also plotted.

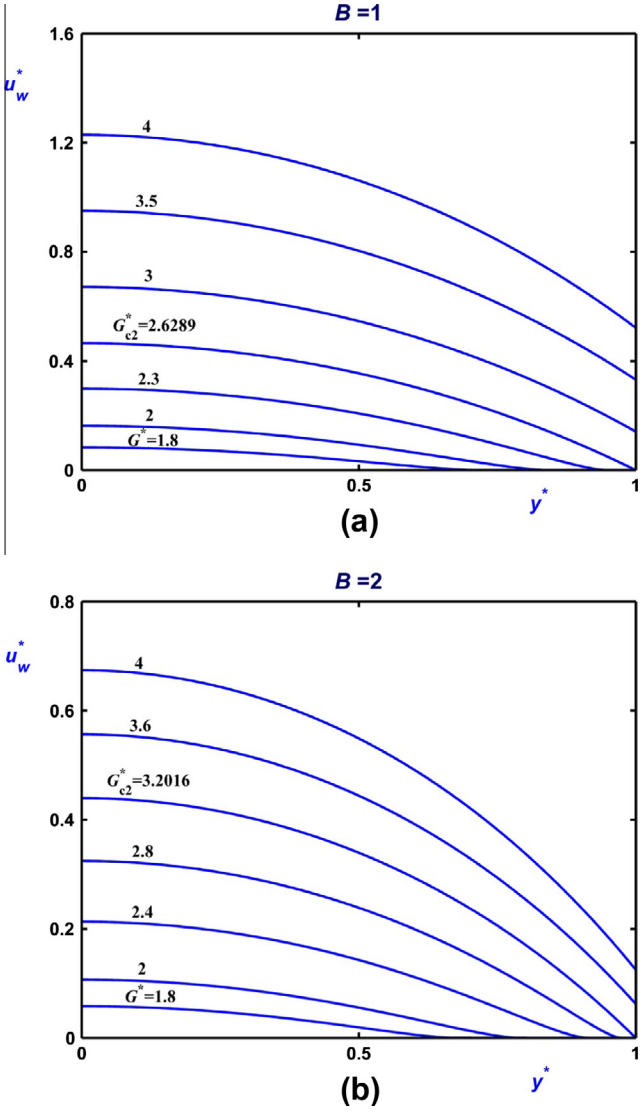

Fig. 4. Slip velocities along the boundary $z^* = 1$ for different values of the imposed pressure gradient in the case of Newtonian Poiseuille flow with non-zero slip yield stress in a square duct ($\alpha = 1$): (a) $B = 1$ and (b) $B = 2$.

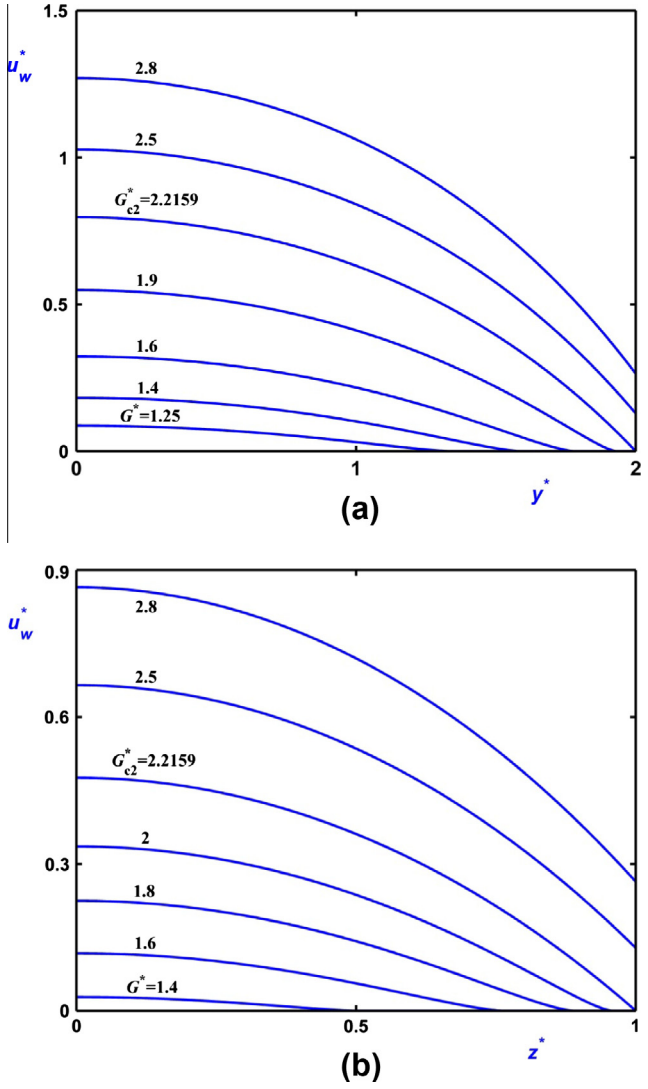

Fig. 5. Slip velocities for different values of the imposed pressure gradient in the case of Newtonian Poiseuille flow with non-zero slip yield stress in a rectangular duct ($\alpha = 2$) with $B = 1$: (a) along $z^* = 1$; (b) along $y^* = 2$.

a critical pressure gradient G_M, which cannot be determined analytically. Eventually, when the pressure gradient exceeds the critical value G_{c2}, slip occurs everywhere (but non-uniformly) along both walls. G_{c2} is determined analytically, as discussed below. It is clear that in the general case of a rectangular duct ($\alpha \neq 1$) there exist four flow regimes, as illustrated in Fig. 2:

(i) For $G \leqslant G_{c1}$, no slip occurs.
(ii) For $G_{c1} < G \leqslant G_M$, partial slip occurs only along the wider wall.
(iii) For $G_M < G \leqslant G_{c2}$, partial slip occurs along both walls.
(iv) For $G > G_{c2}$, non-uniform slip occurs everywhere.

It should be noted that G_M applies when the channel is not square and that no analytical solutions are possible in regimes (ii) and (iii). This is indicated in Fig. 2 with the dashed line in the schematic plot of Q versus G. In the case of a square duct, when $G_{c1} < G \leqslant G_{c2}$ partial slip occurs along both walls (the solution is symmetric). In regime (iv), i.e. for $G > G_{c2}$, the velocity is given by

$$u_x(y,z) = \frac{2c^2 G}{\eta} \sum_{i=1}^{\infty} \frac{\cos(\lambda_i z/c)}{\lambda_i^2(\lambda_i + \sin\lambda_i \cos\lambda_i)} \left[1 - \frac{\cosh(\lambda_i y/c)}{\cosh(\lambda_i \alpha) + \lambda_i \sinh(\lambda_i \alpha)/B}\right] - \frac{\tau_c c}{\eta B} \tag{20}$$

where $B \equiv \beta c/\eta$ (note that this is the inverse of the slip number used by Kaoullas and Georgiou [28]) and $\lambda_i, i = 1, 2, \ldots$ are the roots of

$$\lambda \tan\lambda = B \tag{21}$$

The wall shear stresses along the walls $y = b$ and $z = c$ are respectively

$$\tau_{wy}(z) = 2cG \sum_{i=1}^{\infty} \frac{\sin\lambda_i \cos(\lambda_i z/c)}{\lambda_i(\lambda_i + \sin\lambda_i \cos\lambda_i)[\coth(\lambda_i \alpha) + \lambda_i/B]} \tag{22}$$

and

$$\tau_{wz}(y) = 2cG \sum_{i=1}^{\infty} \frac{\sin^2\lambda_i}{\lambda_i(\lambda_i + \sin\lambda_i \cos\lambda_i)} \left[1 - \frac{\cosh(\lambda_i y/c)}{\cosh(\lambda_i \alpha) + \lambda_i \sinh(\lambda_i \alpha)/B}\right] \tag{23}$$

The minimum wall shear stress occurs at the corners of the rectangular duct. If $\tau_{wy,min} > \tau_c$, slip occurs everywhere. Therefore, the critical pressure gradient G_{c2} above which slip occurs everywhere along all walls corresponds to $\tau_{wy,min} = \tau_{wy}(c) = \tau_c$. Hence,

$$G_{c2} = \frac{\tau_c}{2c \sum_{i=1}^{\infty} \frac{\sin^2\lambda_i}{\lambda_i(\lambda_i + \sin\lambda_i \cos\lambda_i)} \left[1 - \frac{1}{1 + \lambda_i \tanh(\lambda_i \alpha)/B}\right]} \tag{24}$$

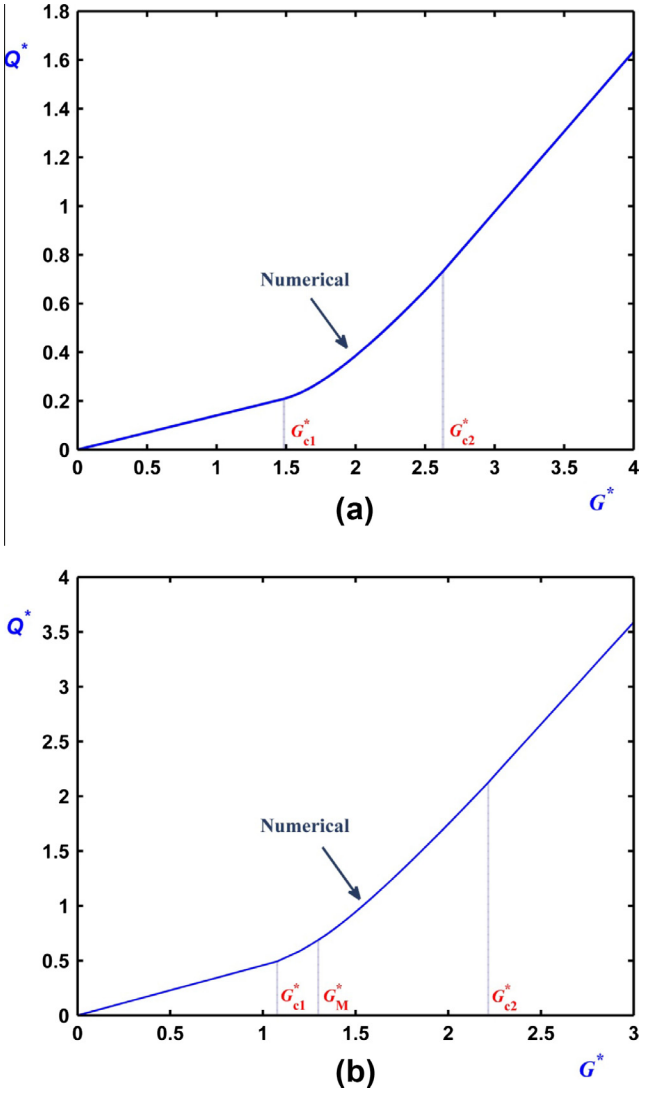

Fig. 6. The volumetric flow rate Q^* in the case of Newtonian Poiseuille flow with non-zero slip yield stress with $B = 1$: (a) square duct ($\alpha = 1$) in which case $G^*_{c1} = 1.4808$ and $G^*_{c2} = 2.6289$; (b) rectangular duct ($\alpha = 2$) in which case $G^*_{c1} = 1.0752$, $G^*_M = 1.2984$ (calculated numerically) and $G^*_{c2} = 2.2159$.

The volumetric flow rate in regime (iv) is given by

$$Q = \frac{8bc^3G}{\eta}\sum_{i=1}^{\infty}\frac{\sin^2\lambda_i}{\lambda_i^4\alpha(\lambda_i+\sin\lambda_i\cos\lambda_i)}\left[\lambda_i\alpha-\frac{\sinh(\lambda_i\alpha)}{\cosh(\lambda_i\alpha)+\lambda_i\sinh(\lambda_i\alpha)/B}\right]-\frac{4\tau_c bc^2}{\eta B} \tag{25}$$

3.1. Non-dimensionalization

For this Newtonian flow, we use a different set of scales, i.e. we scale the velocity by $c\tau_c/\eta$, the pressure gradient by τ_c/c, and y and z by c. The non-dimensionalized velocity and volumetric flow rate are as follows

$$u_x^*(y^*,z^*) = \begin{cases} 2G^*\sum_{i=1}^{\infty}\frac{(-1)^{i+1}}{\alpha_i^3}\cos(\alpha_k z^*)\left[1-\frac{\cosh(\alpha_i y^*)}{\cosh(\alpha_i\alpha)}\right] & G^* \leqslant G^*_{c1} \\ 2G^*\sum_{i=1}^{\infty}\frac{\sin\lambda_i\cos(\lambda_i z^*)}{\lambda_i^2(\lambda_i+\sin\lambda_i\cos\lambda_i)}\left[1-\frac{\cosh(\lambda_i y^*)}{\cosh(\lambda_i a)+\lambda_i\sinh(\lambda_i a)/B}\right]-\frac{1}{B}, & G^* \geqslant G^*_{c2} \end{cases} \tag{26}$$

and

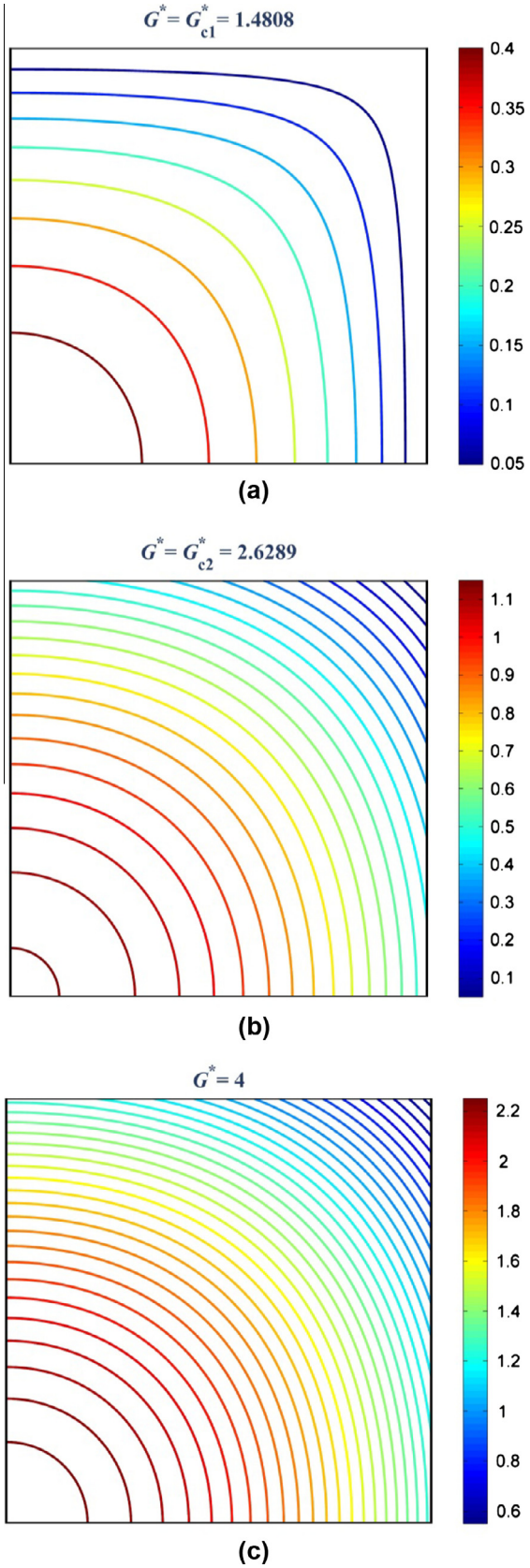

Fig. 7. Numerical and theoretical velocity contours (uniformly distributed values with a step of 0.05) for Newtonian flow with non-zero slip yield stress in a square duct ($\alpha = 1$) with $B = 1$ and different values of the dimensionless pressure gradient.

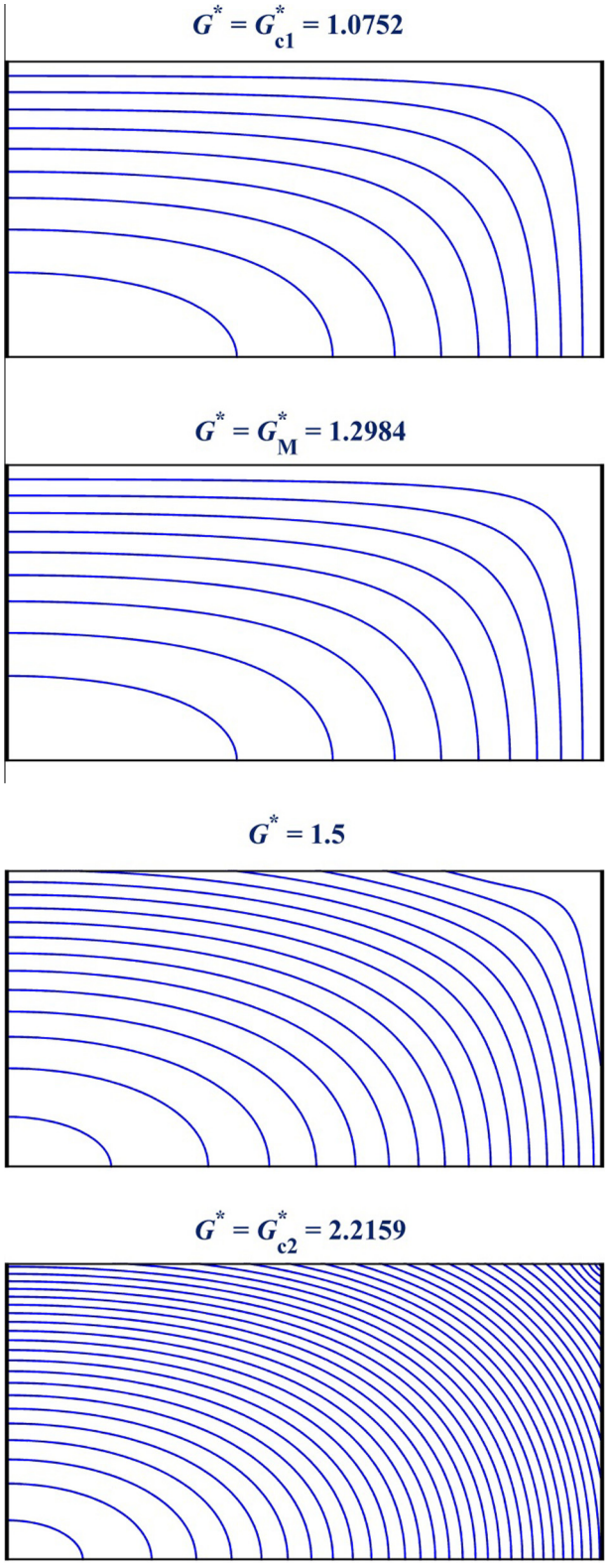

Fig. 8. Numerical velocity contours (uniformly distributed values with a step of 0.05) for Newtonian flow with non-zero slip yield stress in a rectangular duct ($\alpha = 2$) with $B = 1$ and different values of the dimensionless pressure gradient.

$$Q^* = \begin{cases} 8G^* \sum_{i=1}^{\infty} \frac{\alpha_i - \tanh(\alpha_i a)/\alpha}{\alpha_i^4}, & G^* \leqslant G^*_{c1} \\ 8G^* \sum_{i=1}^{\infty} \frac{\sin^2 \lambda_i}{\lambda_i^4(\lambda_i + \sin\lambda_i \cos\lambda_i)} \left[\lambda_i - \frac{\sinh(\lambda_i a)/\alpha}{\cosh(\lambda_i a) + \lambda_i \sinh(\lambda_i a)/B}\right] - \frac{4}{B}, & G^* \geqslant G^*_{c2} \end{cases} \quad (27)$$

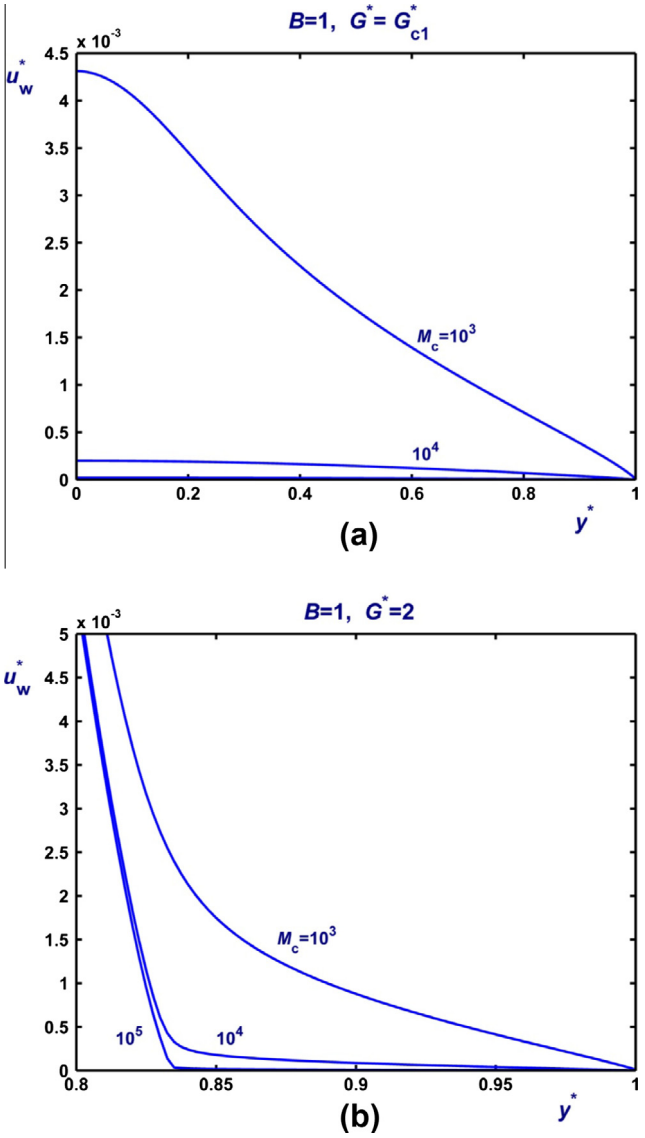

Fig. 9. Effect of the regularization parameter of the slip equation on the slip velocity in Newtonian Poiseuille flow in a square duct ($\alpha = 1$) with $B = 1$: (a) $G^* = G^*_{c1} = 1.4808$; (b) $G^* = 2 < G^*_{c2}$.

where the dimensionless critical pressure gradients are

$$G^*_{c1} = \frac{1}{2\sum_{i=1}^{\infty} \frac{1}{\alpha_i^2}[1 - \operatorname{sech}(\alpha_i a)]} \quad (28)$$

and

$$G^*_{c2} = \frac{1}{2\sum_{i=1}^{\infty} \frac{\sin^2 \lambda_i}{\lambda_i(\lambda_i + \sin\lambda_i \cos\lambda_i)} \left[1 - \frac{1}{1 + \lambda_i \tanh(\lambda_i a)/B}\right]} \quad (29)$$

While G^*_{c1} depends only on the aspect ratio α, G^*_{c2} also depends on the slip number B. As illustrated in Fig. 3, both G^*_{c1} and G^*_{c2} are decreasing functions of α, eventually reaching a plateau. Moreover, G^*_{c2} increases with B and this increase becomes more pronounced at higher values of α. In the extreme case when $B \to 0$ (full slip), $G^*_{c2} \to 1 + 1/\alpha$, which provides a lower bound for G^*_{c2}.

4. Numerical results for the Newtonian flow

The Newtonian case was considered first, in order to obtain solutions in the intermediate regime $(G^*_{c1} < G^* < G^*_{c2})$ where no

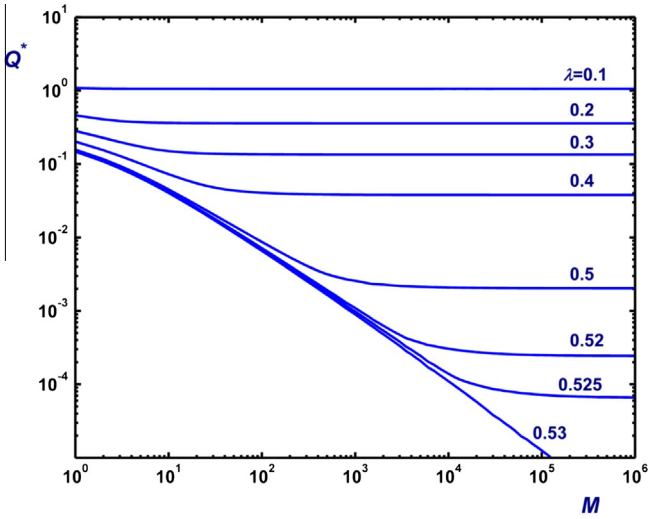

Fig. 10. Volumetric flow rate as function of the dimensionless growth parameter versus $\lambda \equiv 1/G^*$ in the case of Bingham flow in a square duct ($\alpha = 1$) with fixed pressure gradient and no slip at the wall.

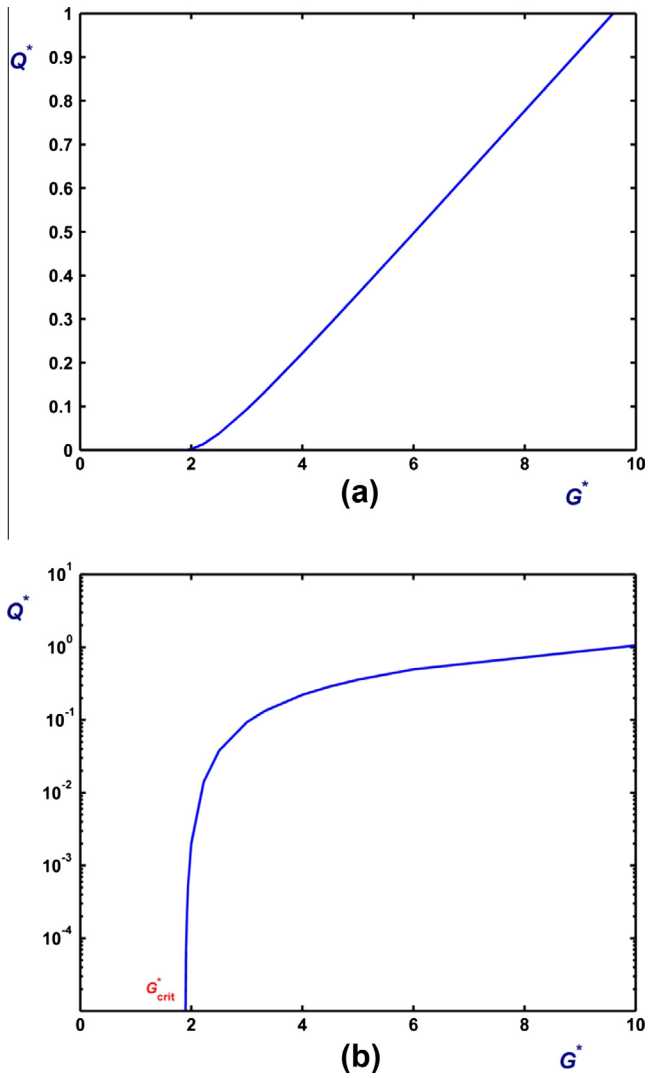

Fig. 11. Volumetric flow rate as function of the imposed pressure gradient in the case of Bingham flow in a square duct ($Bn = 1$, $\alpha = 1$) with no slip at the wall. Flow starts at $G^*_{crit} = 1.8868$.

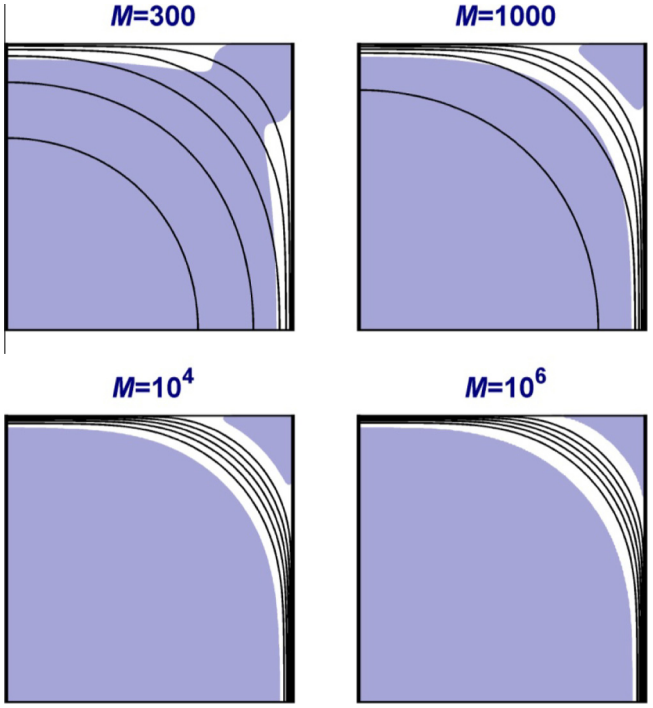

Fig. 12. Unyielded areas (shaded) and velocity contours of Bingham flow in a square duct ($\alpha = 1$) with no slip at the wall for $\lambda = 0.5$ (fixed pressure gradient) and various values of M.

analytical solutions are available and to check the performance of the regularized slip equation. Due to symmetry, the flow problem was solved only in the first quadrant, i.e. in $[0, \alpha] \times [0, 1]$. The finite element method has been used with standard biquadratic elements for the velocity $u_x(y, z)$. A very fine uniform mesh consisting of 200×200 rectangular elements (i.e., 160,801 nodal unknowns) has been used in all calculations for the square duct ($\alpha = 1$); in all other cases ($\alpha > 1$), a uniform mesh of 400×200 elements was used. Simulations have been carried out either at constant volumetric flow rate ($Q^* = 1$) or at a given pressure gradient G^*. In the former case, the pressure gradient is an additional unknown of the problem.

Figs. 4 and 5 show slip velocities calculated for a square ($\alpha = 1$) and a rectangular ($\alpha = 2$) duct, respectively, using different values of the imposed pressure gradient G^* above G^*_{c1}. In Fig. 4, slip velocities along the wall $z^* = 1$ for $B = 1$ and 2 are plotted. The theoretical value of the first critical pressure gradient for the initiation of slip in the middle of the duct wall is $G^*_{c1} = 1.4808$, while slip at the corners starts at $G^*_{c2} = 2.6289$ and 3.2016 for $B = 1$ and 2, respectively. A higher B corresponds to less slip and thus slip velocity is lower for $B = 2$. Similar slip velocity profiles for the Newtonian flow have been presented by Roquet and Saramito [29] who employed the augmented Lagrangian method. In Fig. 5, we plotted the slip velocities along the walls $z^* = 1$ and $y^* = 2$ of the rectangular duct for $B = 1$ and various values of the pressure gradient. In this case, slip at the wider wall is initiated at $G^*_{c1} = 1.0752$ and the critical pressure for having slip everywhere is $G^*_{c2} = 2.2159$. The critical value for the initiation of slip at the midlle of the narrow wall ($y^* = 2$) was determined numerically to be $G^*_M = 1.2984$.

In all cases examined, the numerical slip velocities for $G^* \geqslant G^*_{c2}$ agreed perfectly with the analytical solution. It is easily deduced from Eq. (26) that for any value of a the slip velocity along $z^* = 1$ can be written as follows

$$u^*_w(y^*) = \frac{G^*}{G^*_{c2}} u^*_{w,c2}(y^*) + \frac{1}{B}\left(\frac{G^*}{G^*_{c2}} - 1\right) \tag{30}$$

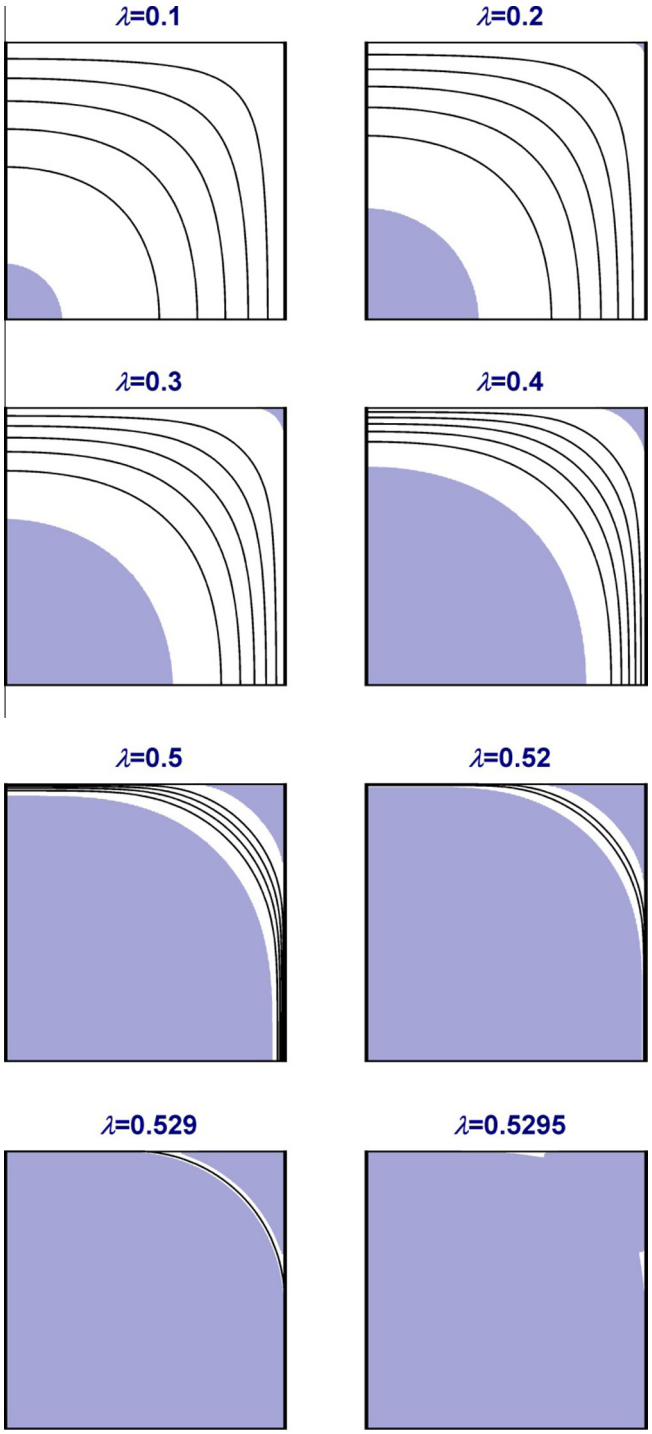

Fig. 13. Unyielded areas (shaded) and velocity contours in the case of Bingham flow in a square duct ($\alpha = 1$) with no slip at the wall for various values of λ (fixed pressure gradient) obtained with $M = 10^6$.

where $u^*_{w,c2}(y^*)$ is the slip velocity for $G^* = G^*_{c2}$. Hence, the slip velocity at the duct corner is simply

$$u^*_w(1) = \frac{1}{B}\left(\frac{G^*}{G^*_{c2}} - 1\right) \tag{31}$$

which provides a convenient test for the validity and convergence of the numerical solution.

In Fig. 6, the volumetric flow rate for $B = 1$ and two values of the aspect ratio ($\alpha = 1$ and 2) is plotted as a function of the imposed pressure gradient G^*. In the no-slip ($G^*_{c1} \leqslant G^*$) and the complete slip ($G^* \geqslant G^*_{c2}$) regimes, Q^* varies linearly with G^* (with a higher slope in the latter case). In the intermediate regime, where no analytical solution exists, Q^* starts increasing more rapidly due to slip. In Fig. 7, the numerical velocity contours for $B = \alpha = 1$ and three values of the dimensionless pressure gradient ($G^* = G^*_{c1}, G^*_{c2}$ and 4) are compared with the analytical ones; in all cases the two solutions are identical. Fig. 8 shows the velocity contours for the case of a rectangular duct ($\alpha = 2$) for $B = 1$ and various values of the pressure gradient.

The effectiveness of the regularized slip equation has been tested for a wide range of the flow parameters, imposing either the pressure gradient or the volumetric flow rate. Of course, much more interesting are the calculations in the regime $G^*_{c1} < G^* < G^*_{c2}$ where there is no analytical solution. Our calculations showed that $M_c = 10^5$ is sufficient for getting accurate results in this regime, with errors much smaller than the tolerance of 10^{-4} used in the numerical code. The effect of M_c is illustrated in Fig. 9 in the case of a square duct ($\alpha = 1$) for $B = 1$ and two values of the imposed pressure gradient, i.e. $G^* = G^*_{c1} = 1.4808$ and $G^* = 2 < G^*_{c2} = 2.6289$. In the former case, there is no slip along the wall and hence the slip velocity should be everywhere zero. As shown in Fig. 9a, if the value of M_c is not sufficiently high, the numerical slip velocity may be finite and higher than the tolerance used in the numerical scheme, especially in the middle of the wall. In the latter case, slip along the wall should be partial, i.e. no-slip in the part of the wall near the corner. As illustrated in Fig. 9b, the sudden change from the slip to the no-slip condition is better captured when $M_c \geqslant 10^5$. All the results presented in the rest of the paper have been obtained with $M_c = 10^5$. Higher values of M_c and extrapolation of the velocity profile are of course required if one needs to obtain accurate estimates of the point of stick–slip transition.

5. Numerical results for Herschel–Bulkley flow

5.1. No wall slip

We first tested the Papanastasiou regularization by obtaining results for Bingham flow in a square duct with no wall slip at fixed pressure gradient G^* and different values of the regularization parameter M. In order to make comparisons with previous works (e.g. [6]), results have been obtained for different values of the parameter

$$\lambda \equiv \frac{1}{G^*} \tag{32}$$

The above parameter is actually the Oldroyd number, $Od \equiv \tau_0/(Gc)$, used by Huilgol and You [18] and others. The effect of M is illustrated in Fig. 10, where the volumetric flow rate is plotted as a function of M for various values of λ. It is clear that above a critical value, λ_{crit}, corresponding to the critical pressure gradient G^*_{crit} for the initiation of flow, Q^* decreases steadily becoming practically zero for a sufficiently high value of M, as it should. For $\lambda < \lambda_{crit}$, Q^* decreases rapidly at low values of M and then tends asymptotically to a finite value. For $\lambda > 0.4$, Q^* appears to converge for moderate values of M, say $M = 1000$. However, as λ approaches λ_{crit}, much higher values of M are necessary in order to obtain converged values of Q^*. Fig. 11 shows the variation of Q^* with G^* when $Bn = 1$ (calculated with $M = 10^6$). The numerical value for the critical pressure gradient is $G^*_{crit} = 1.8868$, which corresponds to $\lambda_{crit} = 0.5295$. The latter value will be discussed in detail below.

The effect of M on the solution is more striking when the unyielded regions ($\tau \leqslant 1$) of the flow are calculated. Fig. 12 shows the calculated unyielded regions and the velocity contours for $\lambda = 0.5$

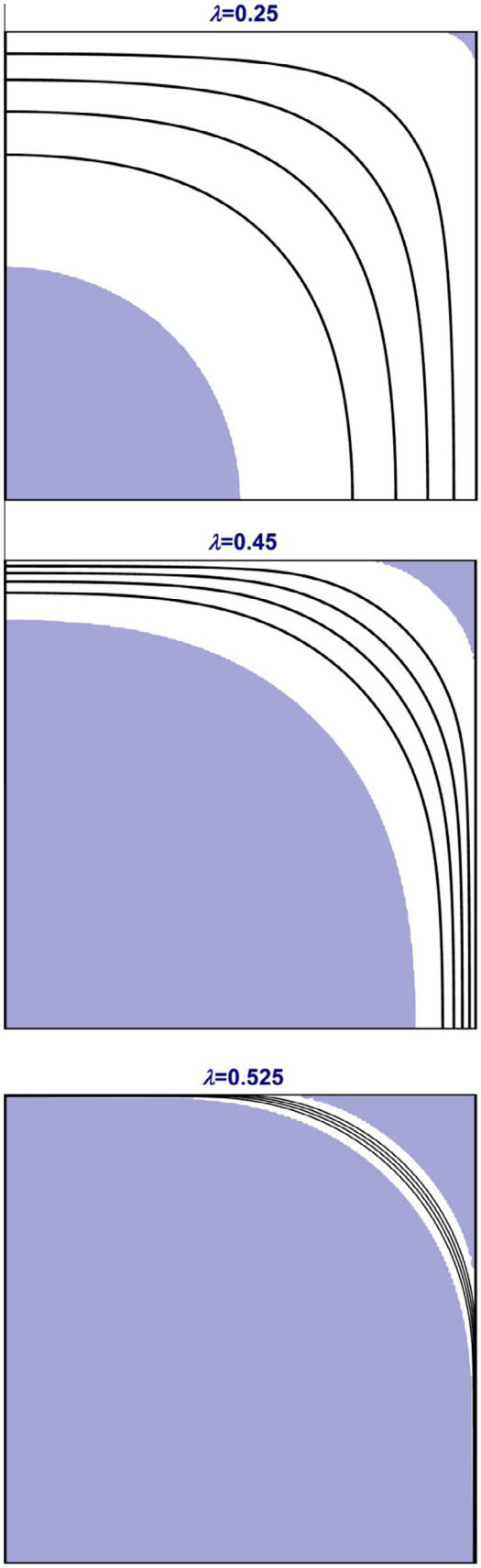

Fig. 14. Unyielded areas (shaded) and velocity contours in the case of Bingham flow in a square duct ($\alpha = 1$) with no slip at the wall for various values of λ (fixed pressure gradient) obtained with $M = 10^6$.

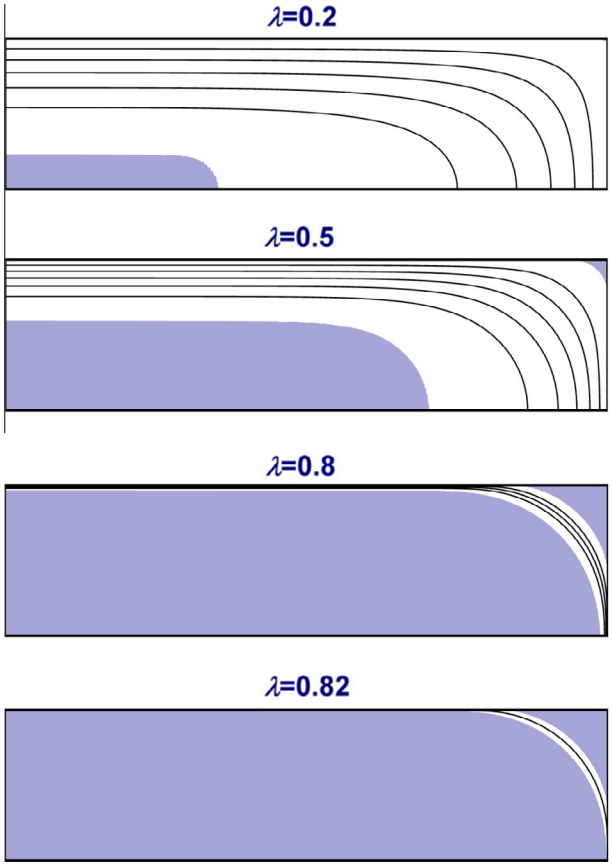

Fig. 15. Unyielded areas (shaded) and velocity contours in the case of Bingham flow in a rectangular duct ($\alpha = 4$) with no slip at the wall for various values of λ (fixed pressure gradient) obtained with $M = 10^6$.

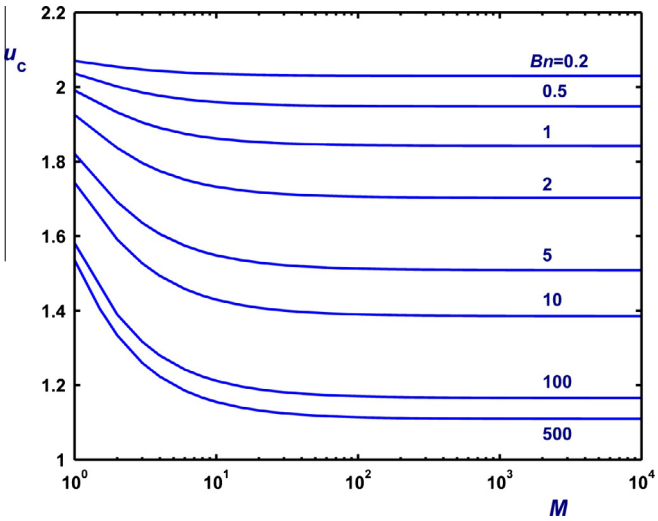

Fig. 16. Maximum velocity (at the center of the duct) versus M for various values of the Bingham number (fixed volumetric flow rate); square duct ($\alpha = 1$), no slip at the wall.

and various values of M. It should be noted that the corresponding Bingham number is rather high, i.e. $Bn = 490.66$. It is clear that the shapes of the unyielded regions change dramatically with M, especially near the duct corner. In fact, the central plug region is initially connected with the stagnant zone in the corner of the duct, which obviously cannot be true. Mosolov and Miasnikov [7–9]

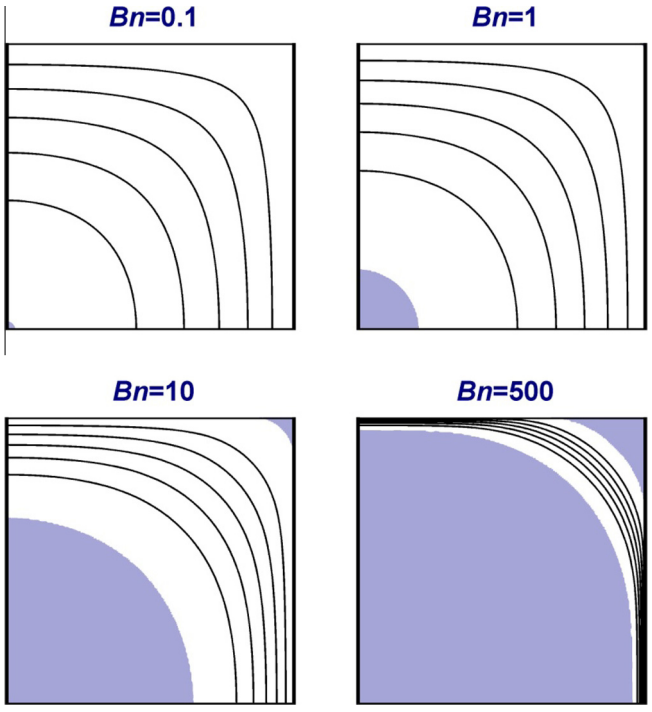

Fig. 17. Unyielded areas (shaded) and velocity contours of Bingham flow in a square duct ($\alpha = 1$) with no slip at the wall for various Bingham numbers (fixed volumetric flow rate) and $M = 10^6$.

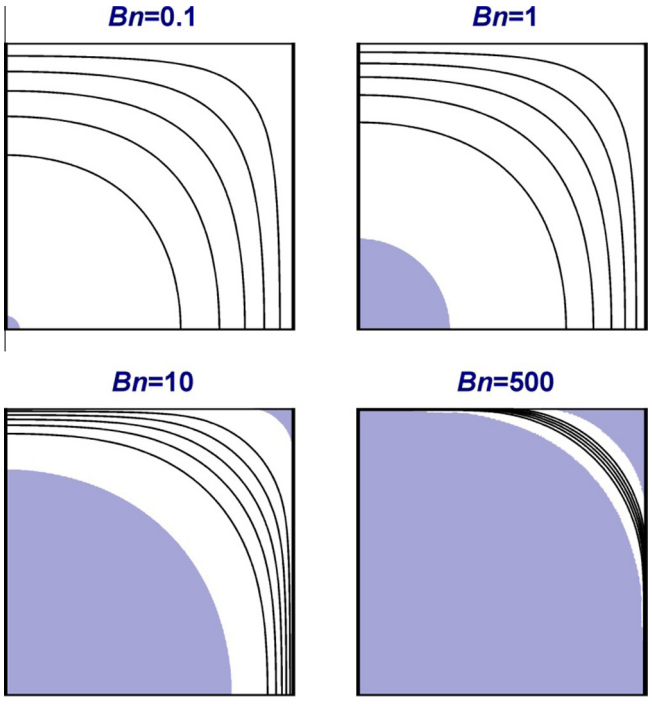

Fig. 18. Unyielded areas (shaded) and velocity contours of Herschel–Bulkley flow in a square duct ($\alpha = 1$) with no slip at the wall for $n = 0.5$ and various Bingham numbers (fixed volumetric flow rate) and $M = 10^6$.

proved that there always exists a core unyielded region and that the boundary of the stagnant zone is always concave toward the stagnant zone. The two regions are separated but yet not converged at higher values of M. Note in particular the tips of the corner yield surfaces the concavity of which is eventually inverted when M is not sufficiently high. It is also clear that when M is not sufficiently high, the velocity in the central "unyielded" region is not uniform (as it should) and the velocity contours may even cross the boundary of that region. Hence, the value of M should be very high in order to obtain acceptable approximations of the ideal Bingham flow. Taylor and Wilson [6] presented results with yielded and unyielded regions for various values of λ (defined as the half of our λ). Because the value of the Bercovier–Engelman regularization parameter was not sufficiently small, the sizes and the shapes of the unyielded regions were not converged, i.e. they look like the present results obtained with a rather low value of M, e.g. $M = 300$, and those of Pham and Mitsoulis [14]. As illustrated in Fig. 12, the plug profile is better captured when $M > 10^4$.

In Fig. 13, we plotted the velocity contours and the unyielded regions for different values of λ (calculated with $M = 10^6$). For small values of λ (i.e. for high pressure gradients), there exists only an unyielded rigid cylindrical core in the center of the duct. As λ is increased (i.e., as the pressure gradient is reduced) the rigid zone decelerates and grows in size. There appears also a small unyielded region near the duct corner, where the material is at rest (stagnant zone). At even higher values of λ, the rigid and the stagnant zones grow further, being separated by thin layer of yielded fluid. The central plug region grows at a faster rate than the corner stagnant zone. Eventually, the two regions merge at λ_{crit} forming a stagnant unyielded body (no flow). According to our calculations the value of λ_{crit} is in the interval (0.5295, 0.53). In this regime, the value $M = 10^6$ is not sufficiently high, as illustrated in Fig. 10 as well as in the last plot of Fig. 13 where the moving rigid core is connected with the stagnant corner zone. Even if a much higher value of M is employed, the values of the velocity are essentially zero, i.e. they are much lower than the tolerance of our numerical calculations, which does not allow the accurate calculation of λ_{crit}.

For the rectangular duct, Mosolov and Miasnikov [7–9] showed that the critical value is given by

$$\lambda_{crit} = \frac{2\alpha}{1 + \alpha + \sqrt{(\alpha - 1)^2 + \alpha\pi}} \tag{33}$$

Hence, in the case of a square duct ($\alpha = 1$), $\lambda_{crit} = 2/(2 + \sqrt{\pi}) \approx 0.53019$. The value $\lambda_{crit} = 0.5295$ calculated in the present work compares well with the analytical value; it is more accurate than other numerical values reported in the literature, despite the fact that the uniform mesh used is not optimal (better

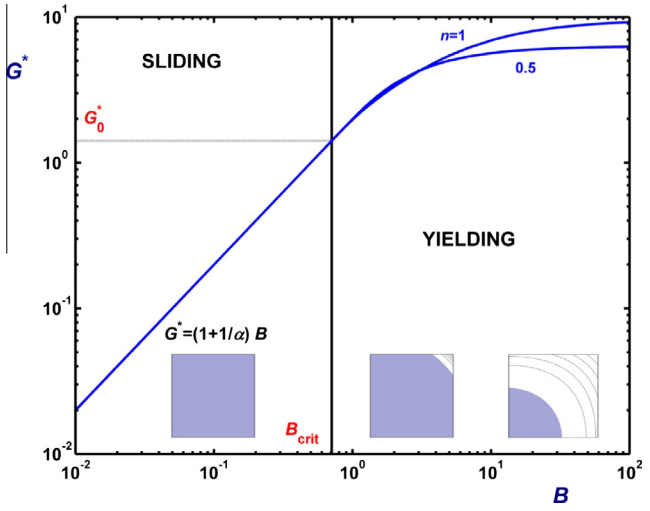

Fig. 19. Calculated pressure gradient as a function of the slip number in the case of Poiseuille flow of a Bingham fluid in a square duct ($\alpha = 1$) with Navier slip. The insets show representative unyielded regions and velocity contours for $n = 1$.

results will be obtained with a graded mesh having the same number of elements). Taylor and Wilson [6] who used a regularization method reported the critical value $\lambda_{crit} = 0.56$. Values obtained by means of the augmented Lagrangian method ranged from 0.52 [18] to as high as 0.66 [35]. Wang [15] and Muravleva and Muravleva [20] reported the values 0.526 and 0.527, respectively. Roquet and Saramito [16] reported initially the value of 0.535 obtained using extrapolation of results for lower values of λ. In a subsequent work, they reported the approximate value $\lambda \approx 0.53$, based on the variation of the maximum velocity [30].

According to theory, at λ_{crit} the yielded region degenerates into a critical curve which is actually a circular arc of radius λ_{crit} [20]. The results for $\lambda = 0.529$ appear to be in good agreement with the theoretical prediction.

In Fig. 14, we plotted the unyielded regions as well as the velocity contours for the three values of λ used in Fig. 11 of the paper of Saramito and Roquet [16], who employed only half of our domain. For $\lambda = 0.25$ and 0.45 the present results are identical to those of Saramito and Roquet [16]. For $\lambda = 0.525$, however, it seems that the predicted yielded region (white) is slightly bigger, which indicates that near λ_{crit}, the value of the regularization parameter is still not sufficiently high. It should be noted, however, that if we demand that at the yield surface $\tau = 1 + \varepsilon$ (instead of $\tau = 1$) and take $\varepsilon = 0.0005$, the predicted unyielded region is essentially the same as that predicted by Saramito and Roquet [16].

A higher aspect ratio, i.e. $\alpha = 4$, has been used in Fig. 15, where the unyielded regions and the velocity contours are plotted for $\lambda = 0.2$, 0.5, 0.8 and 0.82. Note that in this case, one finds from Eq. (33) that $\lambda_{crit} = 0.8295$, which is also the radius of the critical curve for the flow cessation as can be roughly deduced from Fig. 15d.

The effect of the regularization parameter in the other case of interest, i.e. when the volumetric flow rate is imposed, is very similar. As an example, in Fig. 16 the velocity at the center of the duct, u_c, is plotted as a function of M for various values of the Bingham number. The maximum velocity u_c initially decreases rapidly with M and then tends asymptotically to a value approximating the speed of the central unyielded zone of the ideal Bingham flow. The higher the Bn the higher the value of M required for obtaining a converged solution. The fact that in the case of fixed volumetric flow the results appear to be converged say for $M \geqslant 10^3$, which is much smaller than the value of 10^6 proposed for the fixed-pressure-gradient case is not surprising given that the definitions of M are different (see Eqs. (11) and (13)). However, unless otherwise indicated, for all the results of this section the rather high value of 10^6 has been used for M. In Figs. 17 and 18, plots of the unyielded regions and the velocity contours for $n = 1$ and 0.5, respectively, and $Bn = 0.1$, 1, 10 and 500 are shown. Note that when the volumetric flow rate is imposed, the unyielded regions are those where $\tau \leqslant Bn$. By comparing the two figures, one observes that in the shear-thinning case ($n = 0.5$) both the rigid and stagnant zones are bigger in size and the velocity increase in the yielded region is sharper.

5.2. Navier slip

In Poiseuille flows of viscoplastic fluids with Navier slip, the material slides uniformly when the imposed pressure gradient is below the critical value G_0^* at which the material yields, i.e. at a certain part of the flow domain the dimensionless stress exceeds the Bingham number. Hence, for $G^* \leqslant G_0^*$ the velocity is given by $u_x^*(y^*, z^*) = u_w^* = 1$. This then implies that the wall shear stress along both walls is constant, i.e. $\tau_w^* = Bu_w^* = B$. It is also reasonable to assume that in the sliding regime the non-zero shear stresses τ_{yx}^* and τ_{zx}^* vary linearly with y^* and z^*, respectively:

$$\tau_{yx}^* = -\frac{G^*}{1+\alpha} y^* \quad \text{and} \quad \tau_{zx}^* = -\frac{\alpha G^*}{1+\alpha} z^*$$

so that

$$B = \tau_w^* = \frac{\alpha G^*}{1+\alpha}$$

Hence (for a given Bingham number),

$$G^* = \left(1 + \frac{1}{\alpha}\right) B \tag{34}$$

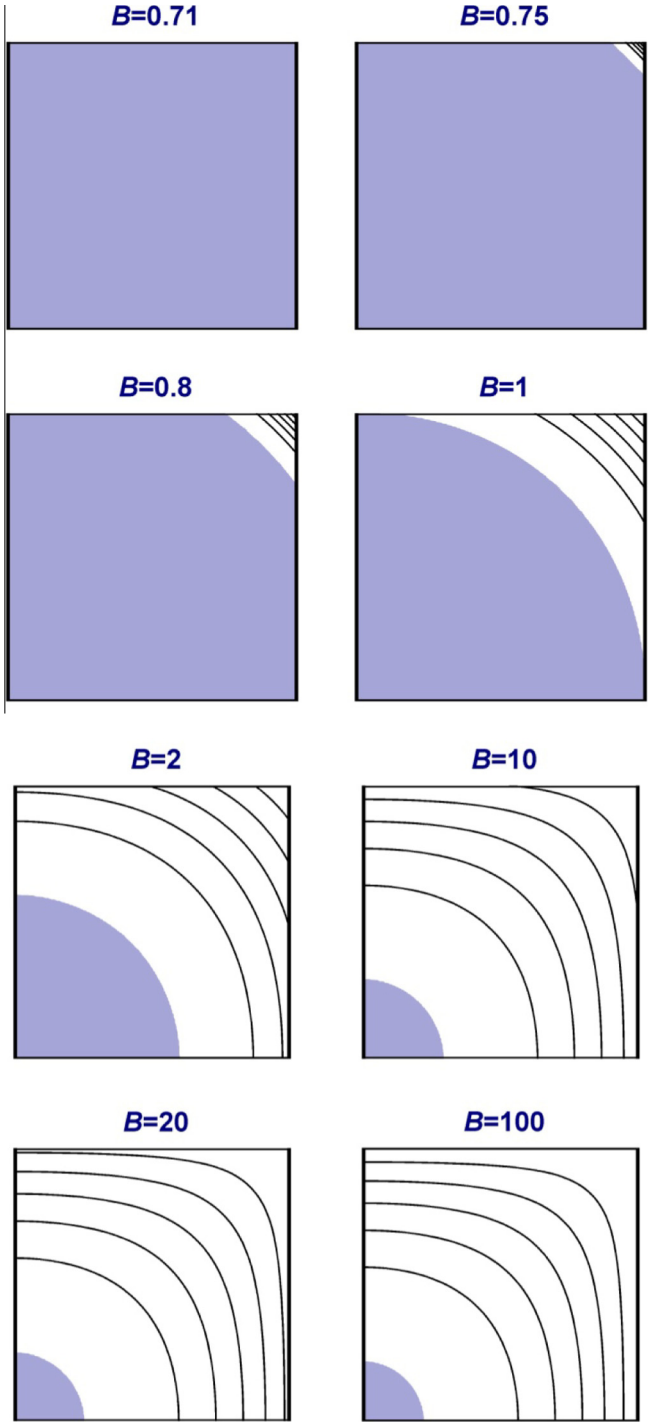

Fig. 20. Unyielded areas (shaded) and velocity contours in the case of Poiseuille flow of a Bingham fluid in a square duct ($\alpha = 1$) with Navier slip for $Bn = 1$ and various slip numbers.

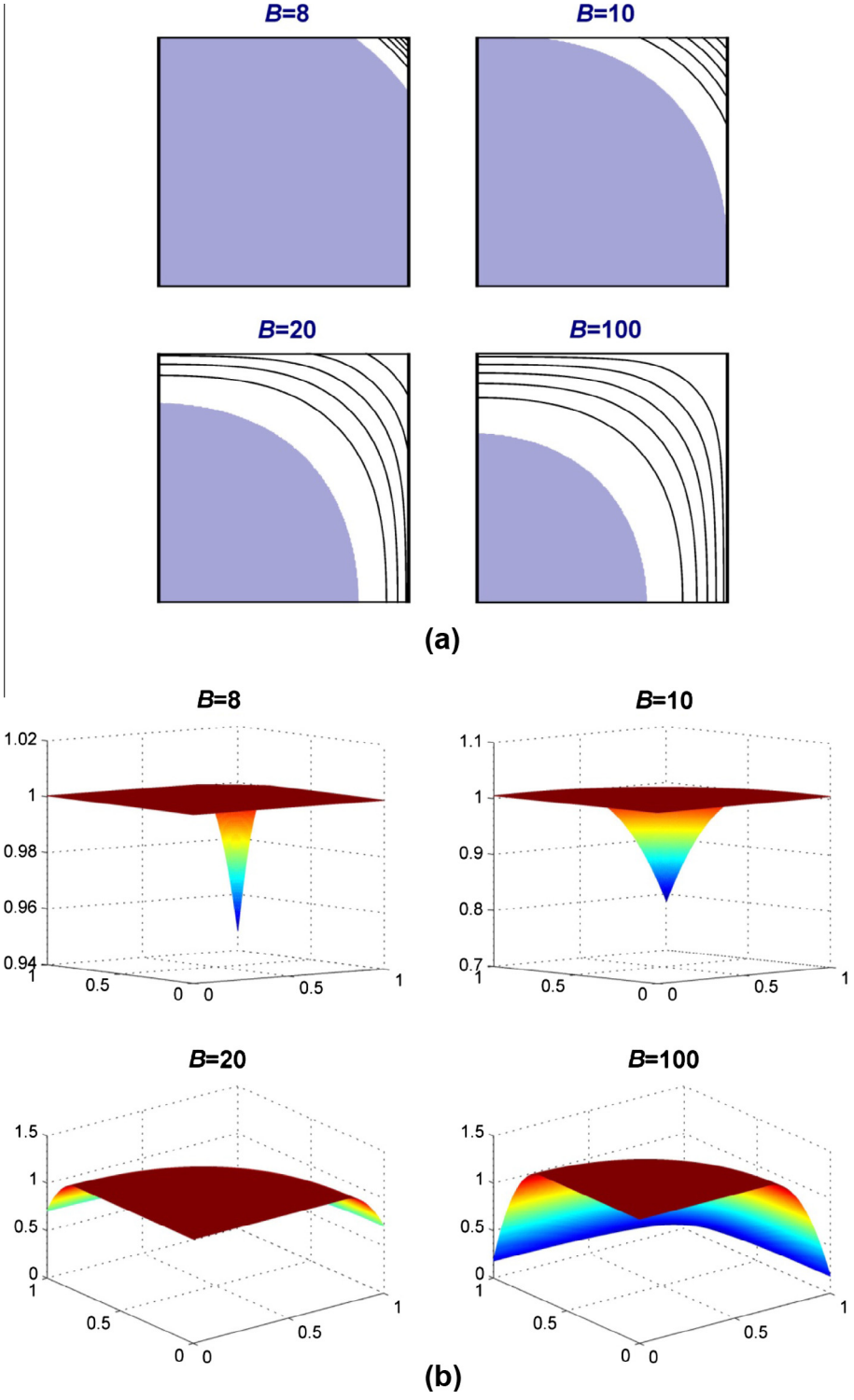

Fig. 21. Bingham flow in a square duct ($\alpha = 1$) with Navier slip at the wall for various slip numbers, $Bn = 10$, and $M = 10^6$: (a) unyielded areas (shaded) and velocity contours; (b) velocity graphs.

The critical value G_0^* can be found by demanding that the maximum stress at the duct corner is $\tau_{max}^* = Bn$. Since, $\tau_{max}^* = \sqrt{2}\tau_w^* = \sqrt{2}B$, one gets the critical slip number below which sliding is observed:

$$B_{crit} = \frac{Bn}{\sqrt{2}} \tag{35}$$

This critical value applies to all viscoplastic fluids with a (constant) yield stress. Therefore, the corresponding critical pressure gradient is

$$G_0^* = \frac{1}{\sqrt{2}}\left(1 + \frac{1}{\alpha}\right)Bn \tag{36}$$

The above quantities are illustrated in Fig. 19, where we actually plotted the numerical predictions of the pressure gradient versus the slip number for $Bn = 1$ and $n = 0.5$ and 1 in the case of a square duct ($\alpha = 1$). Note that the curve for $n = 0.5$ is initially slightly above

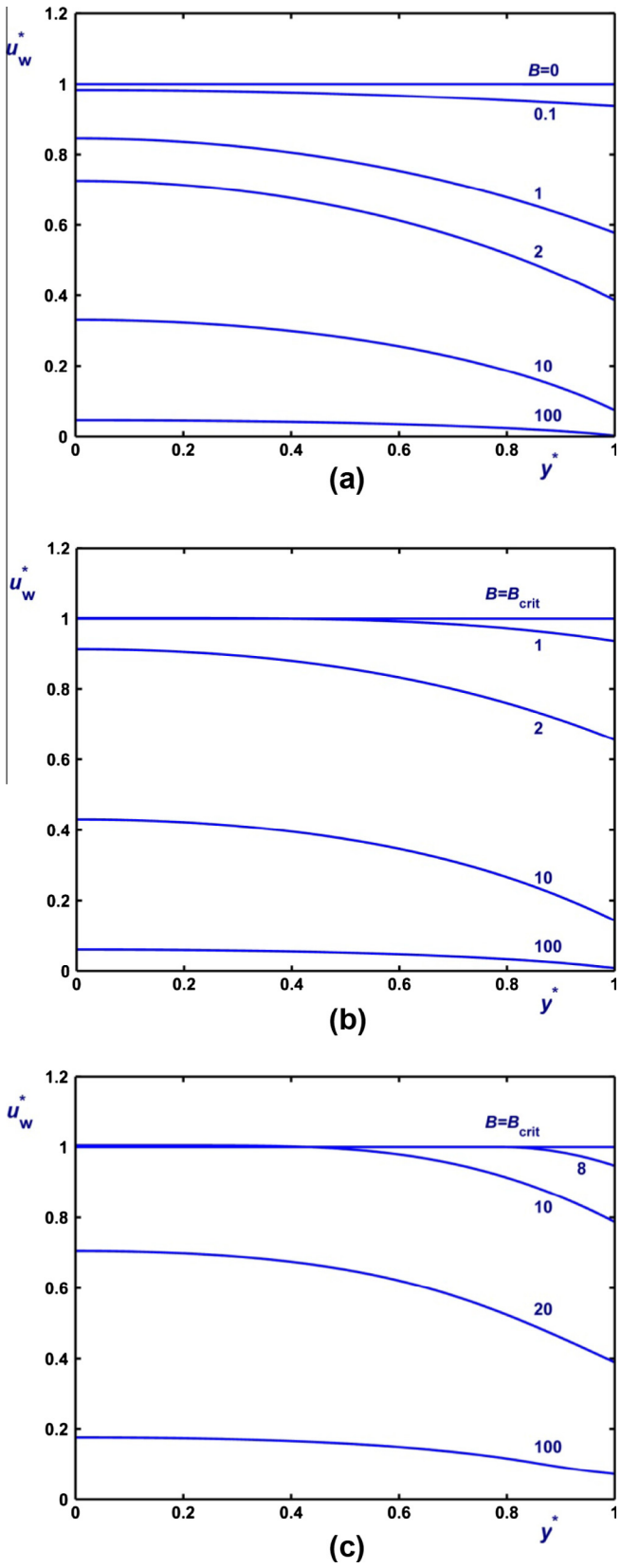

Fig. 22. Slip velocities for various slip numbers in the case of Poiseuille flow in a square duct ($\alpha = 1$) with Navier slip: (a) Newtonian fluid ($Bn = 0$); (b) $Bn = 1$; (c) $Bn = 10$.

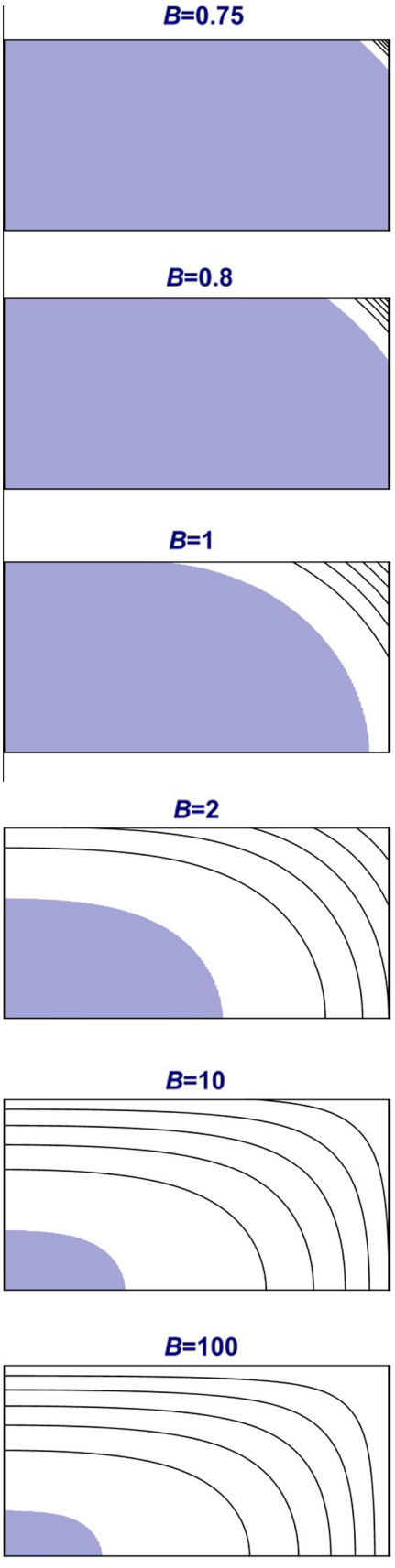

Fig. 23. Unyielded areas (shaded) and velocity contours in the case of Poiseuille flow of a Bingham fluid in a rectangular duct ($\alpha = 2$) with Navier slip for $Bn = 1$ and various slip numbers.

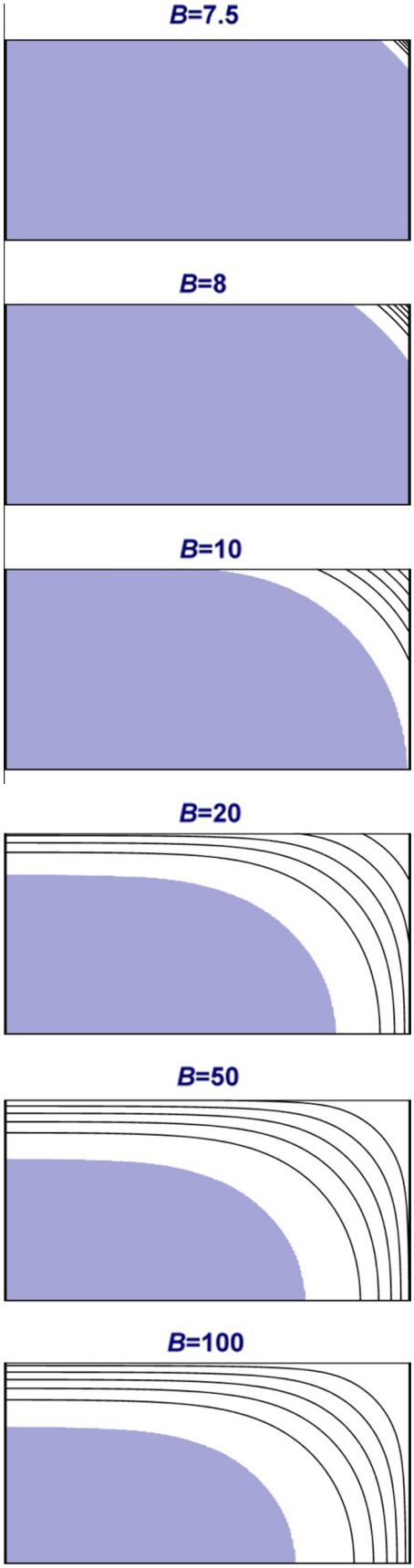

Fig. 24. Unyielded areas (shaded) and velocity contours in the case of Poiseuille flow of a Bingham fluid in a rectangular duct ($\alpha = 2$) with Navier slip for $Bn = 10$ and various slip numbers.

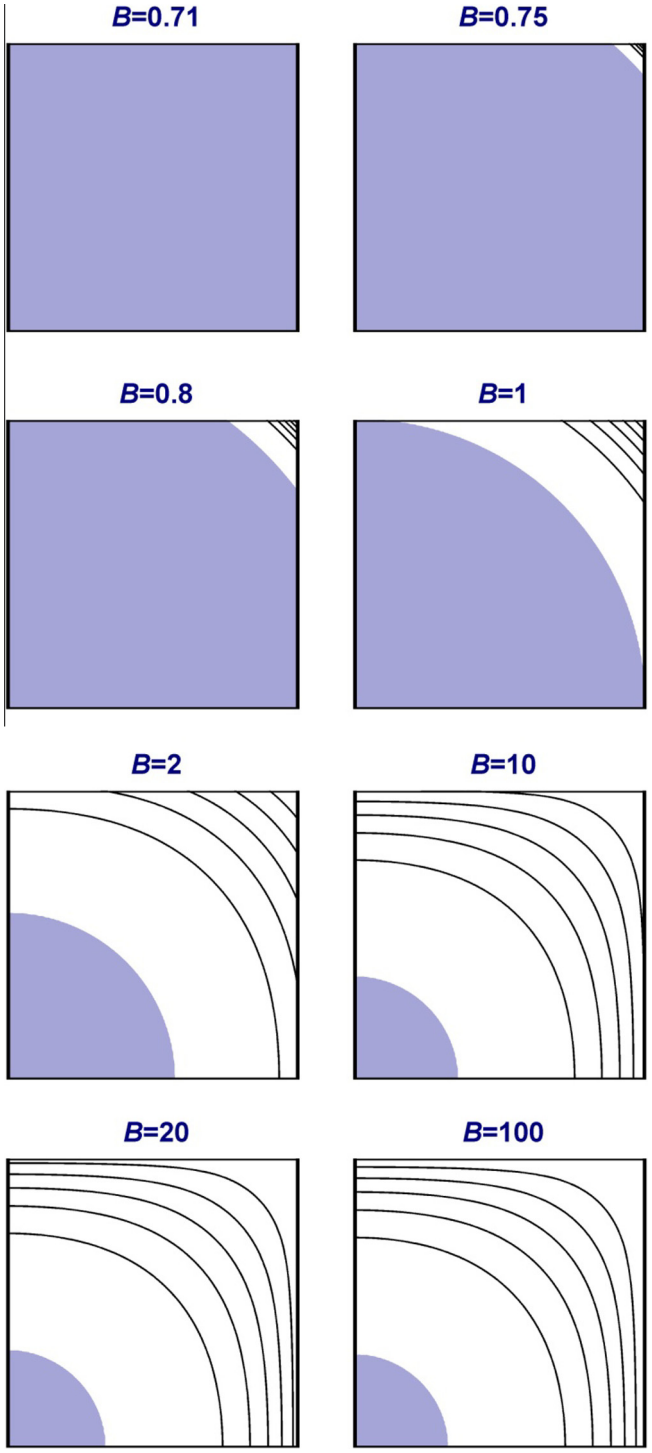

Fig. 25. Unyielded areas (shaded) and velocity contours in the case of Poiseuille flow of a Herschel–Bulkley fluid in a square duct ($\alpha = 1$) with Navier slip for $Bn = 1$, $n = 0.5$ and various slip numbers.

its Bingham plastic counterpart, since at small shear rates the viscosity of the shear thinning fluid is actually higher.

In Figs. 20 and 21, we show the unyielded regions along with the velocity contours in the case of Poiseuille flow of a Bingham fluid in a square duct ($\alpha = 1$) for $Bn = 1$ and 10, respectively, and various slip numbers. For values of B slightly above B_{crit}, most of the fluid is unyielded translating at a constant speed and only a small equilateral triangular yielded region appears near the duct

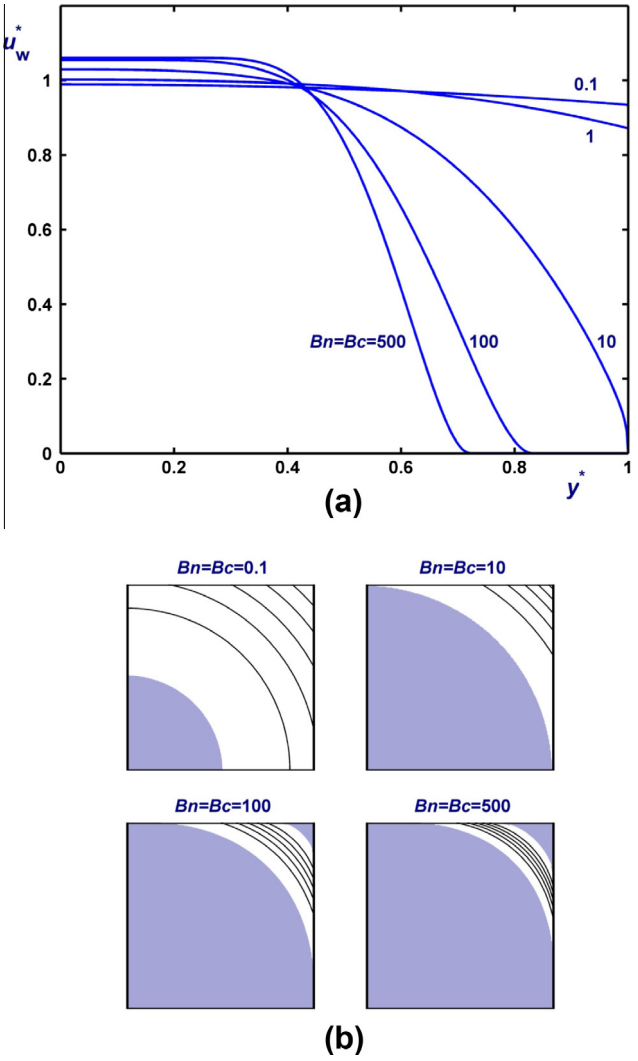

Fig. 26. Poiseuille flow of a Bingham plastic in a square duct ($\alpha = 1$) with non-zero slip yield stress with $B = 0.1$ and various values of $Bn = Bc$: (a) slip velocities; (b) unyielded areas (shaded) and velocity contours.

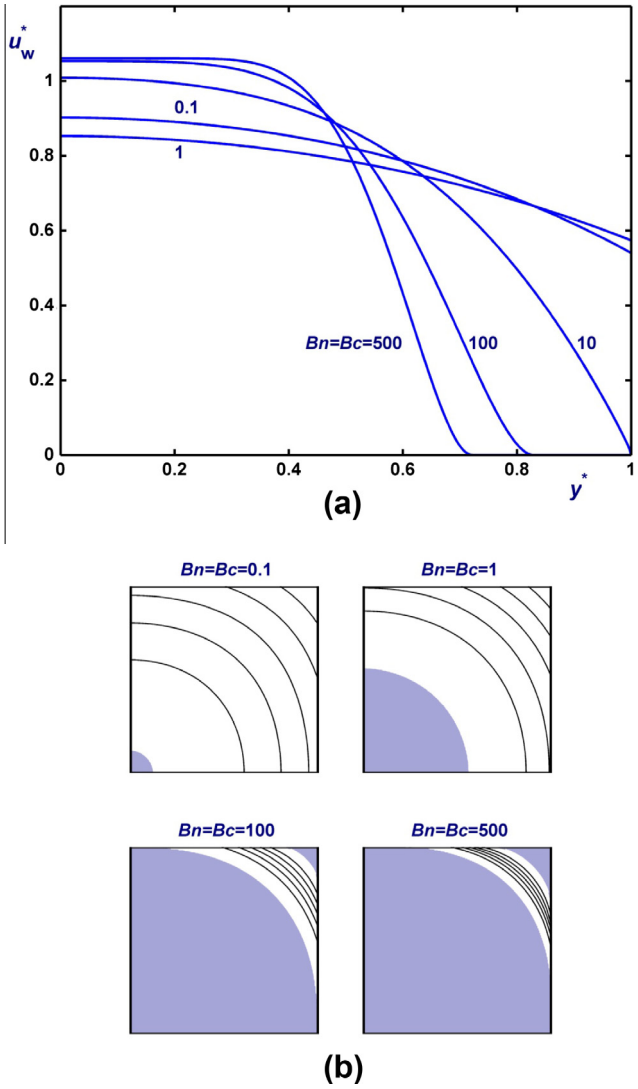

Fig. 27. Poiseuille flow of a Bingham plastic in a square duct ($\alpha = 1$) with non-zero slip yield stress with $B = 1$ and various values of $Bn = Bc$: (a) slip velocities. (b) unyielded areas (shaded) and velocity contours.

corner, in which the velocity contours are straight lines intersecting the walls at a 45° angle. As the slip number is increased the unyielded region shrinks and eventually detaches from the wall and becomes cylindrical. The three-dimensional plots of the velocity in Fig. 21b clearly show the variation of the velocity in the yielded region. Fig. 22 shows the slip velocities $Bn = 0$ (Newtonian), 1, and 10 and for various slip numbers starting from $B_{crit} = Bn/\sqrt{2}$.

Similar results have been obtained for the flow in a rectangular duct, e.g. for $\alpha = 2$, and for other values of the exponent n. Figs. 23 and 24 show the velocity contours and the unyielded areas for $Bn = 1$ and 10, respectively, $\alpha = 2$, and various slip numbers. Note in particular that the shape of the yielded region for values of B just above B_{crit} remains the same (equilateral orthogonal triangle). Fig. 25 shows the unyielded regions as well as the velocity contours obtained for a Herschel–Bulkley fluid with $n = 0.5$, $Bn = 1$ and various slip numbers. As already mentioned the critical slip number for the initiation of deformation is independent of the power-law exponent, i.e. it is the same as that for Bingham flow. A comparison with the Bingham plastic results ($n = 1$) in Fig. 20 shows that the unyielded core is larger and the velocity growth in the yielded zone is faster.

5.3. Slip with non-zero slip yield stress

To simplify things, we restricted ourselves to the case $Bn = Bc$ (i.e., we assume that $\tau_0 = \tau_c$). In Figs. 26–28, we show representative results obtained for three values of the slip number, i.e. for $B = 0.1$ (strong slip), 1 (moderate slip), and 10 (weak slip), and different values of the Bingham number. As shown in Fig. 26a, where we plotted the slip velocity for $B = 0.1$, for small values of Bn (and Bc) slip occurs everywhere along the wall and the slip velocity is initially almost flat. As the value of Bn is increased, the slip velocity is reduced dramatically near the duct corner and is increased slightly near the middle of the wall. Eventually, above a certain critical value of Bn, slip occurs only in the middle of the wall. Moreover, the unyielded area grows and touches the wall. Hence, the slip velocity becomes flat in the middle of the wall where the flow is unyielded and zero near the duct corner. As the Bingham number is increased, another unyielded region appears at the duct corner, which grows in size along with the inner unyielded region. For small values of Bc, the velocity contours are almost circular around the central unyielded region and linear near the duct corner. The shape of the velocity contours in the latter region changes only

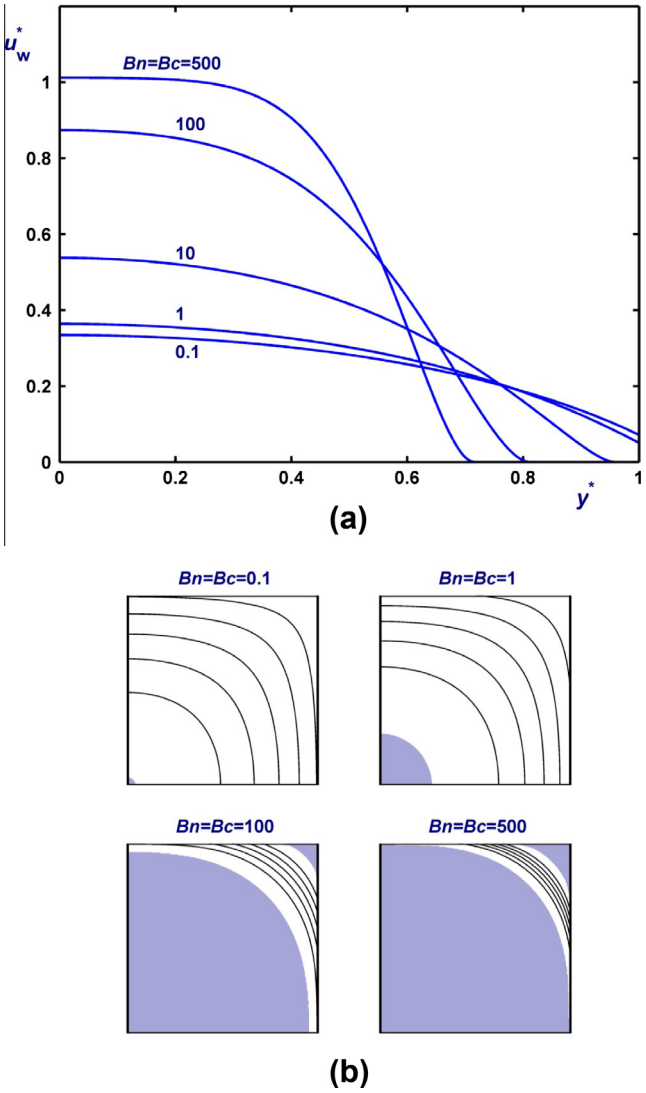

Fig. 28. Poiseuille flow of a Bingham plastic in a square duct ($\alpha = 1$) with non-zero slip yield stress with $B = 10$ and various values of $Bn = Bc$: (a) slip velocities; (b) unyielded areas (shaded) and velocity contours.

when the flow there becomes unyielded. When slip is not strong, e.g. for $B = 1$ in Fig. 27 and $B = 10$ in Fig. 28, the velocity contours in the corner region are bended and tend to become parallel to the wall as slip is reduced. Similar solutions and slip velocity profiles have been presented by Roquet and Saramito [29,30] using the augmented Lagrangian method. It should be noted that in Figs. 26–28, the surfaces of the unyielded regions for $Bn = 100$ and 500 was calculated using the criterion $\tau = Bn + \varepsilon$ with $\varepsilon = 0.01$, since otherwise the yield surface of the corner stagnant zone is incorrect.

6. Conclusions

We used regularized versions of both the constitutive and the slip equations along with finite elements in order to solve the steady-state flow of a Herschel–Bulkley fluid in a rectangular duct with wall slip and non-zero slip yield stress. Using a regularized slip equation with a sufficiently high value of the regularization parameter allows the accurate prediction of the slip velocity, which may be zero along parts of the duct wall and non-zero elsewhere. An advantage over the augmented Lagrangian method is that the same regularization may also be applied to any other non-viscoplastic flows, e.g. other generalized Newtonian or viscoelastic flows, which do not exhibit yielded and unyielded regions. The proposed regularized slip equation has been tested against the analytical solution of the Newtonian flow imposing either the pressure gradient or the volumetric flow rate. Moreover, the results in the intermediate regime of pressure gradients, where slip along the duct wall is partial and no analytical solution is available, were checked by varying the value of the regularization parameter M_c and confirming numerical convergence.

In the case of Bingham flow with no wall slip, it has been demonstrated by means of comparisons with available theoretical results and other numerical results from the literature that regularizing the constitutive equation leads to accurate solutions even for the unyielded regions, provided that the regularization parameter is sufficiently high (of the order of 10^6 and higher). Systematic results have also been obtained in the case of Navier slip (zero slip yield stress) for wide ranges of the Bingham and slip numbers. In the numerical simulations of Bingham flow with non-zero slip yield stress, the latter was taken equal to the yield stress. The effects of the exponent and the aspect ratio have also been examined.

As for the future work, our plan is to solve cessation and start-up flows of a Bingham plastic in pipes of rectangular cross-section with wall slip and non-zero slip yield stress. Muravleva and Muravleva [20] studied the cessation flow of Bingham plastics in ducts with no wall slip. Huilgol [36] analyzed the motion of the yield surface in unsteady shearing flows of viscoplastic fluids and found that this can be considered as a jerk wave, i.e. it is a singular surface across which the velocity, the acceleration and the velocity gradient are continuous, whereas the time derivative of the acceleration, the spatial gradient of the acceleration and the second gradient of the velocity are discontinuous. He also proposed the numerical solution of the start-up Bingham flow in a pipe of square cross-section in order to test the jerk wave hypothesis for the motion of the yield surface.

Acknowledgments

The second author thanks Dr. G. Petekidis (University of Crete) for useful discussions. The project was partially funded by the Greek State (Thales Project "Covisco", MIS 380238) and the Cyprus Research Promotion Foundation (DIAKRATIKES/CY-SLO/0411/02).

References

[1] R.B. Bird, G.C. Dai, B.J. Yarusso, The rheology and flow of viscoplastic materials, Rev. Chem. Eng. 1 (1982) 1–70.
[2] N.J. Balmforth, I.A. Frigaard, G. Ovarlez, Yielding to stress: recent developments in viscoplastic fluid mechanics, Annu. Rev. Fluid Mech. 46 (2014) 121–146.
[3] T.C. Papanastasiou, Flows of materials with yield, J. Rheol. 31 (1987) 385.
[4] M. Bercovier, M. Engelman, A finite element method for incompressible non-Newtonian flows, J. Comp. Phys. 36 (1980) 313–326.
[5] I.A. Frigaard, C. Nouar, On the usage of viscosity regularisation methods for visco-plastic fluid flow computation, J. Non-Newton. Fluid Mech. 127 (2005) 1–26.
[6] A.J. Taylor, S.D.R. Wilson, Conduit flow of an incompressible yield stress fluid, J. Rheol. 41 (1997) 93–101.
[7] P.P. Mosolov, V.P. Miasnikov, Variational methods in the theory of the fluidity of a viscous-plastic medium, PMM, J. Mech. Appl. Math. 29 (1965) 545–577.
[8] P.P. Mosolov, V.P. Miasnikov, On stagnant flow regions of a viscous-plastic medium in pipes, PMM, J. Mech. Appl. Math. 841–854 (1966).
[9] P.P. Mosolov, V.P. Miasnikov, On qualitative singularities of the flow of a viscoplastic medium in pipes, PMM, J. Mech. Appl. Math. 31 (1967) 609–613.
[10] C. Atkinson, K. El-Ali, Some boundary value problems for the Bingham model, J. Non-Newton. Fluid Mech. 41 (1992) 339–363.
[11] R.R. Huilgol, A systematic procedure to determine the minimum pressure gradient required for the flow of viscoplastic fluids in pipes of symmetric cross-section, J. Non-Newton. Fluid Mech. 136 (2006) 140–146.
[12] Y. Wang, Comment on conduit flow of an incompressible yield stress fluid, J. Rheol. 41 (1997) 93–101.

[13] R.R. Huilgol, M.P. Panizza, On the determination of the plug flow region in Bingham fluids through the application of variational inequalities, J. Non-Newton. Fluid Mech. 58 (1995) 207–211.
[14] T.V. Pham, E. Mitsoulis, Viscoplastic flows in ducts, Can. J. Chem. Eng. 76 (1998) 120–125.
[15] Y. Wang, Axial flow of generalized viscoplastic fluids in non-circular ducts, Chem. Eng. Commun. 168 (1998) 13–43.
[16] P. Saramito, N. Roquet, An adaptive finite element method for viscoplastic flows in pipes, Comput. Methods Appl. Mech. Eng. 190 (2001) 5391–5412.
[17] C.O. Faria, J. Karam-Filho, A regularized-stabilized mixed finite element formulation for viscoplasticity of Bingham type, Comp. Math. Appl. 66 (2013) 975–995.
[18] R.R. Huilgol, Z. You, Application of the augmented Lagrangian method to steady pipe flows of Bingham, Casson, and Herschel–Bulkley fluids, J. Non-Newton. Fluid Mech. 128 (2005) 126–143.
[19] E.A. Muravleva, Finite-difference schemes for the computation of viscoplastic medium flows in a channel, Math. Models Comput. Simul. (Engl. Transl.) 1 (6) (2009) 768–779.
[20] E.A. Muravleva, L.V. Muravleva, Unsteady flows of a viscoplastic medium in channels, Mech. Solids 44 (2009) 792–812.
[21] H.A. Barnes, A review of the slip (wall depletion) of polymer solutions, emulsions and particle suspensions in viscosimeters: it causes, character, and cure, J. Non-Newton. Fluid Mech. 56 (1995) 221–251.
[22] S.P. Meeker, R.T. Bonnecaze, M. Cloitre, Slip and flow in pastes of soft particles: direct observation and rheology, J. Rheol. 48 (2004) 1295–1320.
[23] S. Aktas, D.M. Kalyon, B.M. Marín-Santibáñez, J. Pérez-González, Shear viscosity and wall slip behavior of a viscoplastic hydrogel, J. Rheol. 58 (2014) 513–535.
[24] M.M. Denn, Extrusion instabilities and wall slip, Ann. Rev. Fluid Mech. 33 (2001) 265–287.
[25] Y. Damianou, G.C. Georgiou, I. Moulitsas, Combined effects of compressibility and slip in flows of a Herschel–Bulkley fluid, J. Non-Newton. Fluid Mech. 193 (2013) 89–102.
[26] A. Fortin, D. Côté, P.A. Tanguy, On the imposition of the friction boundary conditions for the numerical simulation of Bingham fluid flows, Comput. Meth. Appl. Mech. Eng. 88 (1991) 97–109.
[27] U. Yilmazer, D.M. Kalyon, Slip effects in capillary and parallel disk torsional flows of highly filled suspensions, J. Rheol. 33 (1989) 1197–1212.
[28] G. Kaoullas, G.C. Georgiou, Newtonian Poiseuille flows with slip and non-zero slip yield stress, J. Non-Newton. Fluid Mech. 197 (2013) 24–30.
[29] N. Roquet, P. Saramito, Stick–slip transition capturing by using an adaptive finite element method, Math. Model. Numer. Anal. 38 (2004) 249–260.
[30] N. Roquet, P. Saramito, An adaptive finite element method for viscoplastic flows in a square pipe with stick–slip at the wall, J. Non-Newton. Fluid Mech. 155 (2008) 101–115.
[31] Y. Damianou, M. Philippou, G. Kaoullas, G.C. Georgiou, Cessation of viscoplastic Poiseuille flow with wall slip, J. Non-Newton. Fluid Mech. 203 (2014) 24–37.
[32] J.M. Piau, Carbopol gels: elastoviscoplastic and slippery glasses made of individual swollen sponges: meso- and macroscopic properties, constitutive equations and scaling laws, J. Non-Newton. Fluid Mech. 144 (2007) 1.
[33] C. Métivier, A. Magnin, The effect of wall slip on the stability of the Rayleigh-Bénard Poiseuille flow of viscoplastic fluids, J. Non-Newton. Fluid Mech. 166 (2011) 839.
[34] P. Ballesta, G. Petekidis, L. Isa, W.C.K. Poon, R. Besseling, Wall slip and flow of concentrated hard-sphere colloidal suspensions, J. Rheol. 56 (2012) 1005.
[35] M.A. Moyers-Gonzalez, I.A. Frigaard, Numerical solution of duct flows of multiple visco-plastic fluids, J. Non-Newton. Fluid Mech. 122 (2004) 227–241.
[36] R.R. Huilgol, On the description of the motion of the yield surface in unsteady shearing flows of a Bingham fluid as a jerk wave, J. Non-Newton. Fluid Mech. 165 (2010) 65–69.